

---

## Thirty-four years of Hawaii wave hindcast from downscaling of climate forecast system reanalysis

Li Ning<sup>1</sup>, Cheung Kwok Fai<sup>1,\*</sup>, Stopa Justin<sup>2</sup>, Hsiao Feng<sup>3</sup>, Chen Yi-Leng<sup>3</sup>, Vega Luis<sup>4</sup>,  
Cross Patrick<sup>4</sup>

<sup>1</sup> Department of Ocean and Resources Engineering, University of Hawaii, Honolulu, HI 96822, USA

<sup>2</sup> Laboratoire d'Océanographie Spatiale, Ifremer, Plouzane, France

<sup>3</sup> Department of Atmospheric Sciences, University of Hawaii, Honolulu, HI 96822, USA

<sup>4</sup> Hawaii Natural Energy Institute, University of Hawaii, Honolulu, HI 96822, USA

\* Corresponding author : Cheung Kwok Fai, Tel.: +1 808 956 3485 ; fax: +1 808 956 3498 ;

Email address : [cheung@hawaii.edu](mailto:cheung@hawaii.edu)

[ningli@hawaii.edu](mailto:ningli@hawaii.edu) ; [Justin.Stopa@ifremer.fr](mailto:Justin.Stopa@ifremer.fr) ; [hsiaof@hawaii.edu](mailto:hsiaof@hawaii.edu) ; [yileng@hawaii.edu](mailto:yileng@hawaii.edu) ;

[luisvega@hawaii.edu](mailto:luisvega@hawaii.edu) ; [pscross@hawaii.edu](mailto:pscross@hawaii.edu)

---

### Abstract :

The complex wave climate of Hawaii includes a mix of seasonal swells and wind waves from all directions across the Pacific. Numerical hindcasting from surface winds provides essential space-time information to complement buoy and satellite observations for studies of the marine environment. We utilize WAVEWATCH III and SWAN (Simulating WAVes Nearshore) in a nested grid system to model basin-wide processes as well as high-resolution wave conditions around the Hawaiian Islands from 1979 to 2013. The wind forcing includes the Climate Forecast System Reanalysis (CFSR) for the globe and downscaled regional winds from the Weather Research and Forecasting (WRF) model. Long-term in-situ buoy measurements and remotely-sensed wind speeds and wave heights allow thorough assessment of the modeling approach and the data products for practical application. The high-resolution WRF winds, which include orographic and land-surface effects, are validated with QuickSCAT observations from 2000 to 2009. The wave hindcast reproduces the spatial patterns of swell and wind wave events detected by altimeters on multiple platforms between 1991 and 2009 as well as the seasonal variations recorded at 16 offshore and nearshore buoys around the Hawaiian Islands from 1979 to 2013. The hindcast captures heightened seas in interisland channels and around prominent headlands, but tends to overestimate the heights of approaching northwest swells and give lower estimations in sheltered areas. The validated high-resolution hindcast sets a baseline for future improvement of spectral wave models.

---

## Highlights

► Long-term high-resolution wave hindcast around the Hawaiian Islands. ► Regional winds including orographic effects from Weather Research and Forecasting (WRF). ► Quantification of the complex wave climate in Hawaii. ► Thorough examination of wave hindcast with measurements from 16 buoys and 7 satellite platforms.

**Key words :** Swells ; Wind waves ; Wave hindcast ; Island sheltering ; Spectral wave models ; Weather Research and Forecasting model

## 1. Introduction

---

Hawaii has unique wave climate associated with its North Central Pacific location and massive archipelago. Figure 1 provides a location map to illustrate the prominent wave regimes and geographical features. Extratropical storms near the Kuril and Aleutian Islands generate swells toward Hawaii from the northwest to north during the boreal winter. The south facing shores experience moderate swells from the year-round Southern Hemisphere Westerlies that are augmented by mid-latitude cyclones in the boreal summer. The persistent trade winds generate waves from the northeast to east throughout the year, while subtropical storms during the winter and passing cold fronts can generate waves from all directions. The steep volcanic mountains speed up the wind flows in the channels and create prominent wakes leeward of the Hawaiian Islands (Yang et al., 2005; Nguyen et al., 2010; Hitzl et al, 2014). These localized wind flows together with island sheltering create regional wave patterns with large spatial and temporal variations (Aucan, 2006; Caldwell et al., 2009; Stopa et al., 2011).

There are increasing demands for long-term wave data in support of ocean renewable energy planning, marine ecosystem assessment, shoreline management, and infrastructure development in Hawaii. Altimeters aboard polar orbiting satellites have the advantage of providing significant wave heights with global expanse. The observations are available along satellite tracks at time intervals between 10 and 35 days. The lack of wave direction and period in a multi-modal sea

49 state as well as contamination of the signal by landmasses hamper their application in coastal  
50 regions. Offshore and nearshore buoys have provided in-situ wave measurements at strategic  
51 locations along the island chain as shown in Figure 1. Some of the buoys recorded over 30 years  
52 of wave data and most of the recent measurements are directional. Despite their ability to fully  
53 record the sea state, they are limited to discrete locations and subject to downtime due to  
54 equipment failure and maintenance. A detailed description of the complex wave climate in  
55 Hawaii is best accomplished by numerical modeling, while measurements from altimeters and  
56 buoys are useful for validation of the model results and assessment of the model performance.

57 Third generation spectral wave models, such as WAVEWATCH III of Tolman (2008) and  
58 SWAN (Simulating WAVes Nearshore) of Booij et al. (1999), are proven tools in describing the  
59 multi-modal sea states of Hawaii (Stopa et al, 2011). Despite being developed for open oceans  
60 and shelf seas, WAVEWATCH III is able to depict shadowing of the wave field by the Hawaiian  
61 Islands and heightened seas with small fetches in interisland channels and around headlands  
62 (Stopa et al., 2013; Foster et al., 2014). SWAN is better suited for near-shore environments due  
63 to its efficient implicit scheme to compute wave processes in fine resolution and ability to  
64 account for triad wave interactions in shallow water. Filipot and Cheung (2012) provided  
65 additional parameterizations for energy dissipation due to wave breaking and bottom friction in  
66 the fringing reef environment of Hawaii. The nesting of WAVEWATCH III and SWAN has  
67 proven its effectiveness in modeling wave generation and propagation from the open ocean to the  
68 shore.

69 High-quality global and regional wind forcing is critical for modeling the multi-modal seas in  
70 Hawaii. Reanalysis datasets provide an opportunity to reproduce global wave conditions with  
71 high fidelity (Arinaga and Cheung, 2012; Caires et al., 2004; Chawla et al., 2013; Stopa et al.,  
72 2013). The Climate Forecast System Reanalysis (CFSR) of NOAA NCEP was generated from a  
73 suite of coupled ocean, land, ice, and atmospheric models with assimilation of observations in  
74 three space dimensions (Saha et al., 2010). Its products include hourly surface winds on a  $0.5^\circ$   
75 grid from 1979 to 2010. The same model system produces the CFS version 2 reforecast data with

76 0.205° resolution from 2011 onward as an extension of CFSR (Saha et al., 2014). The ECMWF  
77 Reanalysis (ERA) Interim includes coupling to a spectral wave model and a 4-dimensional  
78 assimilation method (Dee et al., 2011). It has surface wind data every 3 hours with a ~0.7° grid  
79 spacing from 1979 to present. Stopa and Cheung (2014) inter-compared the wind speeds from  
80 CFSR and ERA-Interim with altimetry and buoy observations, and concluded that although both  
81 products have good spatial homogeneity and consistent levels of errors, CFSR provides better  
82 descriptions of the upper percentile winds for wave hindcasting.

83 The orographically induced airflow over Hawaii waters is not resolved by global reanalysis.  
84 The wind flow is significantly modified by steep volcanic mountains of up to 4000 m high and  
85 islands of up to 140 km across as well as the diurnal land-sea thermal contrast (Yang et al., 2005;  
86 Nguyen et al., 2010; Carlis et al., 2010). High-resolution wind data from locally calibrated  
87 atmospheric models is crucial for the wave hindcast around the Hawaiian Islands (Stopa et al.,  
88 2011; 2013). With proper descriptions of lower boundary conditions such as terrain, vegetation  
89 cover, and soil type, high-resolution models have considerable skills in simulating the island-  
90 scale airflow, weather climate, and ocean surface winds (e.g., Zhang et al., 2005; Yang et al.,  
91 2005; Carlis et al., 2010; Nguyen et al., 2010). The Weather Research and Forecasting (WRF)  
92 model of Skamarock and Klemp (2008) has become a standard tool for Hawaii regional climate  
93 studies (Hitzl et al., 2014). The high-resolution WRF model was employed for simulation of a  
94 heavy rainfall event over Oahu associated with a Kona storm and a winter cold front in the mid-  
95 Pacific by Tu and Chen (2011) and Zhou and Chen (2014). The results from these studies were  
96 validated against surface maps, sounding data, and surface measurements.

97 In this paper, we describe a long-term hindcast using WAVEWATCH III and SWAN to  
98 characterize the complex wave climate along the Hawaiian Islands for a 34-year period from  
99 February 1979 to May 2013. Section 2 summarizes the setup of the spectral wave models in a  
100 system of global, regional, and nearshore computational grids. The wind forcing includes CFSR  
101 for the entire globe and downscaled WRF winds for the Hawaii region to account for distant  
102 swells as well as local contributions to the wind waves. A number of error metrics are defined for

103 assessment of the hindcast against measurements from buoys and satellites. In section 3, we  
104 demonstrate the local wave climate through examples of typical wind and wave events from the  
105 hindcast dataset and satellite measurements. These include waves generated by trade winds, a  
106 subtropical cyclone, and a passing cold front as well as a north and a south Pacific swell. Section  
107 4 compares the computed wind and wave data with long-term satellite and buoy observations as  
108 well as previous and existing hindcast datasets. This is followed by a summary of the findings in  
109 Section 5.

## 110 **2. Methodology**

111 We build on the methodology of Stopa et al. (2013), who hindcast the wave conditions  
112 around the Hawaiian Islands with three levels of nested grids using the Final Global  
113 Tropospheric Analysis (FNL) winds for 2000 to 2009. The present model setup involves the  
114 same resolution for Hawaii WAVEWATCH III, but higher resolution for global WAVEWATCH  
115 III and island-scale SWAN. The earlier study utilized the source term package of Tolman and  
116 Chalikov (1996) in WAVEWATCH III version 3.14. There have been advances in the source  
117 term development and implementation (Ardhuin et al., 2010; Banner et al., 2010; Bidlot et al.,  
118 2007; Leckler et al., 2013; Rascle and Ardhuin, 2013; Roger et al., 2012; Tolman et al., 2013;  
119 Zieger et al., 2015). In the present study, we make use of the package of Ardhuin et al. (2010)  
120 with updated descriptions of nonlinear swell dissipation, wave breaking, and wind stress in  
121 WAVEWATCH III version 4.18 (Tolman et al., 2014). The island-scale wave processes are  
122 modeled using the source term of Van der Westhuysen (2007) and Van der Westhuysen et al.  
123 (2007) in SWAN version 40.81, which was modified to include the parameterizations developed  
124 by Filipot and Cheung (2012) for tropical island environments. CFSR, which has improved  
125 physics, assimilation, and resolution compared to FNL, provides the boundary conditions for  
126 Hawaii WRF. This results in more accurate global and regional wind forcing for the wave  
127 models over a longer period from 1979 to 2013. Additional measurements from multiple

128 altimeters and recently deployed near-shore buoys allow for more thorough assessment of the  
129 wave hindcast around the Hawaiian Islands.

### 130 *2.1 Model Setup*

131 We utilize a system of nested global, regional, and island-scale spectral wave models to  
132 capture physical processes at increasing temporal and spatial resolution. Table 1 lists the  
133 coverage and resolution of each computational grid. The global WAVEWATCH III model,  
134 which resolves the oceans from 77.5°S to 77.5°N at 0.5° (~55 km near Hawaii), has a two-way  
135 nested regional grid covering the major Hawaiian Islands at 3 arc-min (~5.5 km) resolution. The  
136 finer regional grid is needed to resolve the wave field in the shadows of the islands (Ponce de  
137 Leon and Guedes Soares, 2005; Stopa et al., 2011). The regional WAVEWATCH III provides  
138 directional wave spectra along the boundaries of the nested SWAN grids around Oahu, Kauai,  
139 Maui and Hawaii Island for modeling of coastal wave transformation with 18 arc-sec (~550 m)  
140 resolution. The multimodal wave conditions are resolved with 50 logarithmic frequency bins and  
141 36 constant directional bins. Figure 1 illustrates the setup of the island-scale nested grids within  
142 the Hawaii regional domain. The island-scale SWAN describes wave transformation over the  
143 insular shelf and around headlands, where high-quality bathymetry comes from a blended dataset  
144 from multibeam and LiDAR surveys (Cheung et al., 2013). The results may in turn define the  
145 boundary conditions for higher-resolution computations of the wave conditions at the shore using  
146 phase-averaged or phase-resolving models (Li et al., 2014).

147 The wind forcing for the wave hindcast comes from CFSR for the entire globe and  
148 downscaled WRF winds for the Hawaii region. The global wind dataset was generated from a  
149 suite of coupled models that includes the Global Forecast System of Yang et al. (2006), the  
150 Modular Ocean Model (MOM) version 4 and sea ice model from the Geophysical Fluid  
151 Dynamic Lab (Griffies et al. 2004), and the NOAA Land Surface Model of Ek et al. (2003) with  
152 assimilation of ground-based, aircraft, ship, and satellite observations (Saha et al., 2010; 2014).  
153 The atmospheric model has 64 vertical layers extending from the surface to 0.2 hPa on a 0.5° (~

154 55 km) grid from 1979 to 2010 and a  $0.205^\circ$  ( $\sim 22.5$  km) grid from 2011 onward. The output  
155 defines the initial and boundary conditions for Hawaii WRF, which is based on a two-way nested  
156 grid system with 38 vertical sigma levels from the surface to 100 hPa (Hitzl et al., 2014). Table 1  
157 includes the horizontal coverage and resolution of the computational grids. The level-1 grid  
158 covers the North Central Pacific at 18 km resolution to accurately model the synoptic weather. It  
159 also provides a transition to the level-2 grid, which resolves the mesoscale wind flows across the  
160 Hawaiian Islands at 6 km resolution. The NOAA Land Surface Model accounts for vegetation  
161 coverage and land surface properties of the Hawaiian Islands using data compiled by Zhang et al.  
162 (2005).

163 The large computational and storage requirements of the 34-year hindcast call for a careful  
164 data management. The pressure, temperature, moisture, and wind velocity from CFSR are  
165 interpolated in space and time to define the initial and boundary conditions for Hawaii WRF. The  
166 production consists of a series of overlapping 36-hour daily runs with the wind velocity output at  
167 the standard 10 m elevation every hour. The first 12 hours allow for model spin-up and the  
168 output from the remaining 24 hours is concatenated to produce a continuous 34-year dataset. The  
169 hourly WRF wind data around the Hawaiian Islands and the CFSR winds for the entire globe are  
170 then interpolated in space and time to define the forcing for wave modeling. The nested global  
171 and Hawaii WAVEWATCH III hindcast comprises 34 overlapping 12.5-month runs with the  
172 first half month for model spin-up and the remaining 12 months for archiving. Parameters such  
173 as significant wave heights, peak periods, and peak directions of the spectral partitions are  
174 archived at all grid points. Two-dimensional wave spectra are only output at buoy locations at  
175 hourly intervals and along boundaries of the four island-scale domains for non-stationary SWAN  
176 computation. The nesting of SWAN in WAVEWATCH III produces higher resolution wave  
177 conditions over the shallow insular shelves and reefs for model validation. The setup also  
178 provides a framework for subsequent modeling of the nearshore wave conditions from the  
179 archived spectral boundary conditions.

## 180 2.2 *Observational Data*

181 QuikSCAT provided wind measurements over 90% of the ice-free ocean surface daily from  
182 1999 to 2009. An onboard scatterometer pulsed cloud-penetrating microwaves in the Ku band  
183 toward the earth and recorded the backscatter signal under a majority of weather conditions. The  
184 wind speed and direction at 10-m elevation are estimated from the backscattered signal using the  
185 Geophysical Model Function along with the Direction Interval Retrieval with Threshold  
186 Nudging (Ebuchi et al., 2002). The polar orbiting satellite flew over Hawaii in ascending and  
187 descending passes. The observations over the 1800-km swath, which covers most of the island  
188 chain, have been post-processed into a spatial grid of approximately 12.5 km resolution to  
189 capture mesoscale wind features (JPL, 2000). The dataset excludes land, coastal, and sea ice  
190 regions and provides rain information for users to remove potentially contaminated data. The  
191 post-processed wind measurements provide a comparison with interpolated data from the Hawaii  
192 WRF model.

193 Significant wave heights detected by actively emitting Ku-microwave signals of satellite  
194 altimeters are instrumental for wave model validation and development (Rascle and Ardhuin,  
195 2013; Stopa et al., 2015; Ardhuin et al., 2010). Once the measured wave heights are quality  
196 controlled and corrected for sensor biases, their accuracy is comparable to buoy measurements  
197 with the advantage of global coverage (Zieger et al., 2009). The GlobWAVE project under the  
198 European Space Agency compiled a comprehensive dataset from multiple platforms (Queffeuilou  
199 and Croize-Fillon, 2010). The data sources include European Remote Sensing 1 (1991-1996) and  
200 2 (1995-2003), Environmental Satellite (2002-2012), Jason 1 (2001-2013) and 2 (2008-present),  
201 Topex-Poseidon (1992-2005), and GEOSAT Follow-on (1998-2008). The GlobWAVE dataset  
202 only includes measurements with strong signal to noise ratio and free from anomalous objects  
203 and landmasses. The standard error is approximately 0.1 m, or 10% of the significant wave  
204 height whichever is larger. The merged along-track measurements cover most of the Hawaii  
205 region from 1991 through 2011 for wave model validation.

206 Hawaii has extensive wave records from a number of buoys for evaluation and validation of  
207 the 34-year hindcast. Table 2 lists the coordinates, water depths, and data periods of 7 offshore  
208 and 9 nearshore buoys considered in this study. We use National Data Buoy Center (NDBC)  
209 numbers to identify the buoys except for Barking Sands, which only has a Coastal Data  
210 Information Program (CDIP) number. The offshore buoys #51001, 51003, 51002, 51004, 51100,  
211 51000, and 51101 around the Hawaiian Island chain have 5-30 years of records and provide  
212 general wave conditions for the validation of the WAVEWATCH III hindcast. Additional wave  
213 measurements are available from nearshore buoys: #39 off west Kauai; #51201, 51202, 51204,  
214 and 51207 around Oahu; #51203 and 51205 off west and north Maui; and #51206 off east  
215 Hawaii (see Figure 1 for location map). Coastal wave measurements are available from KNOH1,  
216 which is a bottom pressure sensor at 12 m water atop a fringing reef on the south shore of Oahu.  
217 Most of the nearshore buoys were deployed after 2010 as part of the Pacific Islands Ocean  
218 Observing System. They detect wave conditions simultaneously on the open and lee sides of an  
219 island or island group for validation of the SWAN results and examination of the model  
220 capability in describing wave conditions around the islands.

### 221 *2.3 Error Metrics*

222 The recorded and hindcast datasets have different spatial and temporary resolutions. We  
223 post-process the hindcast data to match the record location and time stamp and compile data pair  
224 sequences for direct comparison. A number of error metrics available to measure the difference  
225 between the two datasets. These include the mean error or bias and the root-mean-square error,  
226 defined as

$$227 \quad ME = \frac{1}{n} \sum_{i=1}^n (y_i - x_i) \quad (1)$$

$$228 \quad RMSE = \sqrt{\frac{1}{n} \sum_{i=1}^n (y_i - x_i)^2} \quad (2)$$

229 where  $(x_i, y_i)$  denote the recorded and hindcast data pairs and  $n$  is the number of data pairs. The  
230 overall agreement can be illustrated by the correlation coefficient and scatter index as

$$231 \text{ COR} = \frac{\sum_{i=1}^n (y_i - \bar{y})(x_i - \bar{x})}{\sqrt{\sum_{i=1}^n (y_i - \bar{y})^2} \sqrt{\sum_{i=1}^n (x_i - \bar{x})^2}} \quad (3)$$

$$232 \text{ SI} = \frac{1}{\bar{x}} \sqrt{\frac{1}{n} \sum_{i=1}^n [(y_i - \bar{y}) - (x_i - \bar{x})]^2} \quad (4)$$

233 where the over bar indicates time average.

234 A scatter plot of the data pairs can illustrate the general relationship between the records and  
235 hindcast to complement the error matrices. A regression line can provide additional insight by  
236 showing the variation of the bias over the data range. The time lag between recorded and  
237 hindcast events might contribute to the scatter of the data even with good agreement of the  
238 magnitude. We use the quantile-quantile (Q-Q) plots to compare the percentile distributions of  
239 the two datasets independent of the time stamps. It should be noted that the records also contain  
240 errors and are used as a reference for comparison.

### 241 **3. Hawaii Wave Climate**

242 Hawaii experiences persistent trade winds and episodic cold fronts throughout the year, as  
243 well as occasional Kona Storms in the winter months. These events generate wind waves with 6  
244 to 12 sec period that are mixed with long-period swells from north and south Pacific  
245 extratropical cyclones. An understanding of the underlying processes and local features is  
246 necessary to identify the strengths and weaknesses of the hindcast. Although the sea state is  
247 typically multi-modal, we select representative wind wave and swell events from the 34-year  
248 dataset to illustrate the Hawaii regional wind and wave climate. Satellite observations allow  
249 assessment of the hindcast in capturing the selected events as well as their spatial patterns  
250 introduced by the island chain.

251 Trade wind waves are the most common, especially during the summer months, when the  
252 subtropical high to the north of Hawaii is strong and stable. Figure 2 shows a typical trade wind

253 and wave event on 17 August, 2005. The geopotential height at 300 mb indicates the presence of  
254 a subtropical high-pressure over an area to the north of Hawaii setting up a regime of persistent  
255 trade winds toward the islands. Hawaii WRF and QuikSCAT at the nearest time stamp show  
256 trade winds of  $5\sim 7\text{ m s}^{-1}$  from the northeast as well as deceleration in front of the islands and  
257 acceleration in channels and around southern Hawaii Island. WRF produces more refined  
258 features of the wind field especially in the wake of Hawaii Island. QuikSCAT cannot fully  
259 capture these small-scale processes with a spatial resolution of  $\sim 12.5\text{ km}$ . The trade winds  
260 generate waves with 1.5 m significant wave height and 8 s peak period from the east. The  
261 acceleration of the trade winds in the channels and south of Hawaii Island augments the local  
262 wave height to 2.2 m. The altimeter observation from GlobWAVE at the nearest time stamp  
263 validates the approaching wave heights as well as the heightened seas associated with local  
264 acceleration of the winds. Shadows of the wind waves develop leeward of the islands and expose  
265 a long-period south swell of less than 1 m wave height in the background.

266 The local trade wind flow is occasionally interrupted by cold fronts passing through the  
267 Hawaiian Islands from the west to east over a period of several days. Figure 3 shows the  
268 atmospheric and wave conditions when a cold front approached Hawaii on March 1, 2004. The  
269 300-mb geopotential height indicates a migrating trough to the northwest of Hawaii. Under these  
270 synoptic weather conditions, a low-level cyclonic flow is generated over Kauai and Oahu as seen  
271 in the QuikSCAT and WRF wind fields (half an hour apart). The winds transition from  $15\text{ m s}^{-1}$   
272 northerly to under  $10\text{ m s}^{-1}$  southeasterly across the island chain. The simulated southeasterly  
273 winds produce wakes off the north-facing shores of Maui and Hawaii Island with speed under 3  
274  $\text{m s}^{-1}$ . QuikSCAT detects the reduction of the wind speed but cannot resolve the detailed airflow  
275 in the wakes. The migrating cold front generates northwest waves across the ocean reaching  
276 Hawaii with 2.5 m height and 13~14 s period that are evident south of the island chain. These  
277 together with locally generated southeast waves and trade wind waves from the far field produce  
278 a multi-modal sea state with 3 m wave height and 9 s period to the north. In comparison to the  
279 altimetry data, the hindcast reasonably describes the wave height increase from south to north

280 across the island chain as well as sheltering effects southwest of Maui and southeast of Hawaii  
281 Island.

282 Some of the migrating upper-level troughs may develop into subtropical cyclones known  
283 locally as "Kona Storms" during the winter (Simpson 1952). Once developed, a Kona storm  
284 moves erratically and can generate winds toward Hawaii from any direction. There are, on  
285 average, two to three Kona storms per year (Otkin and Martin, 2004). Figure 4 shows a selected  
286 event, which occurs on December 5, 2007 for illustration. The 300-mb geopotential height  
287 indicates a trough axis with closed contours north of Kauai that generates a Kona storm over the  
288 North Central Pacific. Both QuikSCAT and the WRF winds resolve the low-level circulations  
289 associated with the Kona storm and a strong converging flow across Oahu and Maui on its  
290 southeastern flank. The waves reach 6 m height and 10 s period within the core and attenuate  
291 toward the east and south following the tail of a northwest swell passing through the islands.  
292 Locally generated short-period waves from the converging flow are evident to the south of Maui  
293 and Oahu, which are in the shadow of the swell. The altimeter captured a cross section of the  
294 storm waves and swell with heights corroborating the hindcast results. The erratic motions of  
295 Kona storms can generate severe wave conditions on coastlines that are typically sheltered from  
296 trade winds and swells. For infrastructure planning and development, these events must be taken  
297 into consideration as they might produce more severe waves for a given coastline.

298 In addition to waves associated with local weather, Hawaii also experiences large swells  
299 generated by North Pacific extratropical cyclones during the winter months and moderate swells  
300 from the South Pacific throughout the year. Figure 5 provides an illustration of a south swell  
301 mixed with east wind waves on July 12, 2001. The approaching swell with 2.1 m significant  
302 wave height and 15 s peak period produces shadows north of the island chain, where trade wind  
303 waves with 1.8 m height and 7.6 s period are evident. The multimodal sea state is augmented by  
304 the heightened wind waves downstream of the channels and around southern Hawaii Island. The  
305 altimetry measurements validate the heights of the computed south swell and wind waves and  
306 confirm the heightened conditions south of the islands as well as the shadows immediately to the

307 north. Comparing to the south swells, the north Pacific swells approaching Hawaii are more  
308 energetic. The direction, which is typically from the northwest, switches to the north at the end  
309 of the winter season. Figure 6 illustrates a prominent shadow along the Hawaiian Islands created  
310 by a northwest swell on January 5, 2001. The swell with 3.5 m significant wave height and 15 s  
311 peak period is dominant north of the islands. Background wind waves can be seen in the  
312 shadows southeast of Hawaii Island and at the Alenuihāhā Channel. In comparison to the  
313 altimetry measurements, the hindcast reproduces the swell to the north of the islands as well as  
314 the wave height variation in the shadow to the south.

315 The five case studies have illustrated the typical components of Hawaii's wave climate.  
316 Empirical orthogonal function (EOF) analysis of the CFSR wind and wave datasets has shown  
317 strong dependence of the swells and trades wind waves on the El Niño Southern Oscillation  
318 (Stopa and Cheung, 2014). El Niño years usually have increasing frequency and intensity of  
319 north swells (Aucan, 2006), but weaker trade winds and reduced Kona storm activity (Caruso  
320 and Businger, 2006; McPhaden et al., 2006). In addition to interannual climate cycles, the wind  
321 waves and swells in Hawaii are influenced by long-term climate change. Fyfe (2003) and Yin  
322 (2005) showed polarward intensification of the extratropical cyclones in the Southern and  
323 Northern Hemispheres in recent decades and into the 21st century. O'Connor and Chu (2015)  
324 showed 44% decrease of Kona Lows and 23% decrease of cold fronts for the La Niña years from  
325 the 1956-1982 to the 1983-2010 epoch. The buoy records from around Hawaii indicate shifting  
326 of trade winds from northeast to east during the 1980s to 2000s epoch (Garza et al., 2012).  
327 Through satellite and buoy records, reanalysis datasets, and model simulations, Boisséson et al.  
328 (2014) showed robust strengthening of trades winds over the Pacific during the past 20 years.  
329 The swells and wind waves reflect the changing extratropical cyclone, local storm and trade  
330 wind patterns. After validation with available observations, the 34-year high-resolution hindcast  
331 provides a wealth of information for studies of interannual cycles and long-term climate change  
332 as well as their impact to Hawaii.

#### 333 **4. Assessment of Hindcast**

334 We have illustrated the spatial patterns of typical wind and wave events around the Hawaiian  
335 Islands. The main features include heightened winds and waves in channels and around southern  
336 Hawaii Island as well as relatively calm conditions on the lee side of the islands. The selected  
337 events qualitatively demonstrate the capability of the hindcast in describing the complex sea  
338 states, which have significant implications for the marine environment and coastal infrastructure.  
339 With the typical spatial patterns identified, we now provide quantitative assessment and  
340 validation of the 34-year hindcast dataset in terms of the error metrics against long-term satellite  
341 and buoy measurements.

##### 342 *4.1 Validation with Satellite Data*

343 Satellite observations allow validation of the complex spatial patterns of the hindcast around  
344 the Hawaiian Islands. The year-round trade winds have seasonal patterns influenced by the  
345 location of the subtropical high north of Hawaii. Figure 7 compares the average surface winds  
346 from WRF and QuikSCAT in the summer months of June, July and August and the winter  
347 months of December, January, and February during 2000 to 2009. The subtropical high is  
348 directly northeast of Hawaii in the summer. WRF shows average trades of  $6\sim 8\text{ m s}^{-1}$  from the  
349 east-northeast with maximum reaching  $11\text{ m s}^{-1}$  in the Alenuihaha Channel and relatively calm  
350 conditions in the wake of Hawaii Island. The subtropical high migrates toward the northeast  
351 Pacific in the winter. The trade winds weaken and shift to a more easterly direction. The more  
352 compact winds have an average speed of  $3\sim 8\text{ m s}^{-1}$  approaching Hawaii. WRF reproduces the  
353 gridded QuikSCAT winds in the winter, but slightly underestimates the open ocean wind speed  
354 by approximately  $0.5\text{ m s}^{-1}$  during the summer months. The seasonal pattern in QuikSCAT also  
355 depicts accelerated flows and wakes leeward of the islands, but the wakes are not as prominent  
356 as those from WRF likely due to the coarse resolution of 12.5 km. In addition, QuikSCAT is

357 known for overestimation of the wind speed under weak and variable conditions (Pensieri et al.,  
358 2010; Satheesan et al., 2007).

359 The hourly WRF winds with 6 km resolution are interpolated in time and space to match the  
360 QuikSCAT data over a 12.5-km grid for computation of the error metrics. Figure 8 shows the  
361 spatial distributions of the mean error, root-mean square error, correlation coefficient, and scatter  
362 index of the WRF winds from 2000 to 2009. Kona storms and cold front are less frequent and the  
363 error metrics primarily reflect the persistent trade wind conditions in Hawaii. The simulated  
364 high-resolution wind data from the WRF model reproduces the approaching flow as well as the  
365 local acceleration in the channels and south of Hawaii Island with less than  $0.4 \text{ m s}^{-1}$  mean error  
366 and  $2 \text{ m s}^{-1}$  root-mean-square error. The corresponding correlation coefficient of 0.7~0.8 and  
367 scatter index below 0.2 indicate good agreement between the two datasets in time. The most  
368 significant discrepancy occurs in the wake region of Hawaii Island, where the mean and root-  
369 mean-square errors reach  $-2$  and  $3.8 \text{ m s}^{-1}$ , due to overestimation of the wind speed by  
370 QuikSCAT. The low correlation and large scatter in the wake region indicate the challenge in  
371 modeling of the stochastic processes and remote-detection of the weak, variable flows. Since the  
372 fetch is small and the wind speed is low, the wake is not a significant generation region that  
373 influences the local wave climate.

374 The wave conditions in Hawaii are highly localized due to orographically induced airflows as  
375 well as sheltering of both the wind waves and swells by the islands. GlobWAVE, which includes  
376 altimeters with multiple ground tracks over the Hawaii region, provides a consolidated dataset of  
377 significant wave height to assess the spatial pattern of the hindcast. Figure 9a shows the locations  
378 of altimetry observations from 1991 to 2011. The observations adjacent to large landmasses,  
379 which have high noise to signal ratio, were omitted in the dataset. We linearly interpolate the  
380 5.5-km hindcast data in space to match the altimetry record of the nearest hour for comparison.  
381 The hindcast and recorded data pairs are binned onto a spatial grid for computation of the error  
382 metrics. Figure 9b shows the grid coverage and the number of data pairs in each bin. The grid  
383 resolution of  $0.25^\circ$  is selected to provide an optimal balance between the data density and spatial

384 resolution. The use of multiple platforms over a period of 21 years provides adequate coverage  
385 of the waters around the Hawaiian Islands. Bins along tracks of long-running satellites have up to  
386 3410 data pairs, and those with less than 30 data pairs are not considered in the computation of  
387 the error metrics.

388 Figure 10 shows the mean error, root-mean square error, correlation coefficient, and scatter  
389 index to provide an indication of the wave model performance around the Hawaiian Islands. The  
390 distribution of the error metrics is influenced by the trade wind waves as well as the north and  
391 south swells. Kona storms and cold fronts, which can generate severe wave conditions, are less  
392 frequent with negligible influence on the statistics. The mean error shows overestimation of the  
393 significant wave height north and south of the island chain and underestimation in the shadows  
394 of the northwest swells and trade wind waves. The small error to the southeast of Hawaii Island  
395 alludes to accurate reproduction of the trade wind waves. The RMSE follows a similar pattern,  
396 but with slightly larger values to the south likely due to the varying shadow region associated  
397 with the change of swell direction from northwest to north during the winter season. The high  
398 correlation coefficient and low scatter index north and east of the island chain indicate the  
399 hindcast captures the timing of the approaching north swell and wind waves reasonably well.  
400 The lower correlation and large scatter immediately south and west of the islands reflect the  
401 limitation of the spectral models in reproducing the wave conditions in sheltered regions. This is  
402 most evident in the region west of Hawaii Island, which is in the shadow of both the northwest  
403 swells and trade wind waves.

#### 404 *4.2 Validation with Buoy Data*

405 The offshore and near-shore buoys around the Hawaiian Islands provide hourly  
406 measurements of the wind and wave conditions and several of them were in operation during  
407 most of the hindcast period. The detailed in-situ measurements complement the remotely sensed  
408 data for validation of the hindcast. Hitzl et al. (2014) validated the simulated high-resolution  
409 surface winds from the WRF model with records from 11 offshore and nearshore buoys for 2000

410 to 2009. The computed speeds have a bias within  $-0.9$  to  $0.4$   $\text{m s}^{-1}$  and RMSE of  $1.6$  to  $3.1$   $\text{m s}^{-1}$   
411 among the 11 sites during the summer months, when the trade winds are strong and the  
412 conditions are challenging to the model. The results are consistent with the QuikSCAT  
413 comparison in Figure 8. The highest errors occur at a buoy downstream of Maui and Lanai in the  
414 wake of the trade wind flow.

415 The wave buoys provide the significant wave height and peak period and the recent  
416 measurements include the peak direction as well. Figure 11 shows, for example, the comparison  
417 of the hindcast wave parameters with available measurements at 6 selected offshore and  
418 nearshore buoys in 2012 (see Figure 1 for location map). The hindcast reproduces the seasonal  
419 variations as well as the individual events, albeit the gaps in the records when the buoys were  
420 not in operation. Both datasets at the three offshore buoys indicate persistent east wind waves of  
421  $1\sim 3$  m significant wave height and  $6\sim 10$  s peak period along the Hawaiian Islands. The records  
422 at buoy #51101 northwest of Kauai also show large north swells reaching 7 m and 21 sec in the  
423 winter months. The wave height decreases to 5 m at buoy #51002 south of the island chain due  
424 to sheltering of the north Pacific swells. Buoy #51004 southeast of Hawaii Island is open to the  
425 north, but recorded slightly smaller wave heights because the island chain blocks the more  
426 energetic swells from the northwest. Although swells from the South Pacific reach Hawaii all  
427 year round, their low energy levels are often masked by the more energetic north swells or wind  
428 waves and have little influence on the peak period or direction at the offshore buoys. During the  
429 summer, the hindcast shows significant wave height of over 4.5 m at Buoys #51002 and #51004  
430 due to Hurricane Daniel, which only affected the waters south of the island chain.

431 The records at the three nearshore buoys show distinct wave climate on the north, east, and  
432 south sides of Oahu. Buoy #51201 located 9 km off the north shore recorded comparable swell  
433 conditions to #51101 with significant wave height and peak period up to 6.3 m and 22 s in the  
434 winter. Wind waves of 1 to 2 m height and 5 to 10 s period from the northeast reach the buoy  
435 during the summer. Buoy #51202 off the east shore is open to wind waves from the northeast to  
436 east, but is partially sheltered from the more energetic northwest swells. The hindcast model

437 reproduces the persistent wind waves of 1~3 m height, but underestimates the intermittent swells,  
438 which reach 4.2 m in the records. Buoy #51204 is sheltered from the majority of the north  
439 Pacific swells except those passing through Ka'ie'ie Channel from the northwest. The hindcast  
440 model resolves the period and direction of the northwest swells reasonably well, but  
441 underestimates the height likely due to the low spatial resolution, which cannot fully describe the  
442 steep seafloor near the buoy. Since the buoy is sheltered from direct approach of the northeast  
443 wind waves during the summer, it recorded clear signals of the south swell with 0.6~1.8 m  
444 height and up to 22 s period for validation of the hindcast.

445 We compile the scatter plots of the hindcast significant wave height against all available  
446 buoy data from 1979 to 2013 for an overall assessment. Figure 12 provides the scatter plots of  
447 the two datasets at the six selected buoys. The results at the three offshore buoys demonstrate the  
448 model performance in different regions around the island chain. The hindcast predicts the  
449 recorded wave height reasonably well with 90% of the data within  $\pm 0.68$  m and small RMSEs of  
450 0.29~0.47 m. The apparent large scatter for the energetic events is due to offset of the northwest  
451 swell arrivals between the hindcast and buoy measurements. The timing offsets are consistent for  
452 the exposed buoys leading to the similar scatter indices of 0.16 and 0.17 at buoys #51101 and  
453 buoy #51002 in the northwest and southwest regions. Buoy #51004, sheltered from the northwest  
454 swells by the island chain, yields a smaller scatter index of 0.12. Consistent with the altimetry  
455 comparison, the mean error at buoys #51101 and 51002 shows a positive bias of 0.16-0.28 m due  
456 to the northwest swell. The bias reduces to 0.06 m at buoy #51004 in the shadow of Hawaii  
457 Island. The regression lines with slopes of 0.87 to 0.99 and the high correlation coefficients up to  
458 0.91 indicate good overall agreement between the hindcast and recorded wave heights at the  
459 offshore locations.

460 The wave conditions at the nearshore buoys around Oahu are mostly influenced by local  
461 island features. Buoy #51201 off the north shore is exposed to northeast wind waves and north  
462 Pacific swells and the scatter plot shows a pattern similar to that of the offshore buoy #51101  
463 with the regression slope close to one. The smaller overall wave height and mean error are due to

464 partial sheltering of the energetic northwest swells by Kauai and the east trade-wind waves by a  
465 prominent headland on northeast Oahu. The small RMSE of 0.36 m and the high correlation  
466 coefficient of 0.92 indicate good quality of the hindcast at this relatively exposed location. Buoy  
467 #51202 off the east shore experiences smaller wave heights due to sheltering of the northwest  
468 swells by the same headland. While most of the error metrics are comparable to those off the  
469 north shore, the ME improves from 0.18 to -0.01 m associated with dominance of the trade wind  
470 waves instead of the northwest swells. Buoy #51204 southwest of the island experiences the  
471 mildest wave conditions among the three nearshore buoys due to sheltering from the majority of  
472 the north Pacific swells and trade wind waves. This buoy is exposed to year-round south swells  
473 with typical significant wave heights of around 1 m. The negative mean error of -0.06 m  
474 indicates overall underestimation of the hindcast wave height. The small 0.65 regression slope  
475 implies greater underestimation of the energetic northwest swell events reaching the site. The  
476 low correlation of 0.78 is likely due to the limitations of the model in resolving the northwest  
477 swells and trade wind waves at this sheltered location.

478 The Q-Q plots eliminate the timing errors and compare directly the percentile distributions of  
479 the hindcast and recorded significant wave heights. Figure 13 provides the comparisons at the six  
480 selected buoys. The hindcast at the three offshore buoys shows good accuracy for wave heights  
481 up to 5 m that account for at least 98% of the occurrence. The model tends to overestimate wave  
482 heights above 5 m at the exposed buoys #51101 and 51002, but underestimate at buoy #51004  
483 southeast of Hawaii Island in the shadow of the northwest swells. The extreme wave heights at  
484 the two exposed buoys are associated with Kona storms or cold fronts and are well captured by  
485 the hindcast due to the proximity of the buoys to the sources. The same pattern also exists at the  
486 nearshore buoys around Oahu. The hindcast yields slight overestimates of the wave height at the  
487 exposed buoy #51201, but shows underestimation at the sheltered buoys #51202 and 51204 for  
488 wave heights above 5 and 1.5 m, which correspond to the 99.6 and 85 % percentiles respectively.  
489 The lower predictions of the energetic events at #51202 are due to the model limitations in  
490 describing wave transformation around obstacles and in the shadows of islands. The hindcast at

491 buoy #51204 shows underestimation beginning at a smaller wave height and a lower percentile  
492 because of its location in the shadows of both the north Pacific swell and northeast trade wind  
493 waves.

494 The time series, scatter, and Q-Q plots from the six selected buoys have illustrated the  
495 relationships between the hindcast and recorded datasets at the regional and island scales. Table  
496 3 summarizes the error metrics from the 16 buoys based on all available measurements. Ninety  
497 percent of the hindcast wave heights are within  $\pm 0.69$  m or less of the measurements, except for  
498 buoy #39, which only recorded episodic events. The mean error at the offshore buoys #51000,  
499 51001, 51003, 51100, and 51101 and the nearshore buoys #39, 51201 and 51205, which are  
500 exposed to north Pacific swells, shows a consistent positive bias of 0.10 to 0.37 m. Buoy #51002  
501 south of the island chain is sheltered from the late season north swell. Its comparable ME of 0.16  
502 m implies the consistent positive bias comes from the more energetic and frequent northwest  
503 swells. The offshore buoy #51004 and the nearshore buoys #51202, 51207, and 51206, which are  
504 partially sheltered from the northwest swells, show negligible or small MEs of -0.01 to 0.06 m.  
505 The nearshore buoys KNOH1, #51203, and 51204, which are at well-sheltered locations from the  
506 north Pacific swells and northeast trade wind waves, show negative biases of -0.06 to -0.12 and  
507 low correlation coefficients of 0.67 to 0.78. The hindcast at these locations also shows strong  
508 tendency to underestimate the large events as indicated by the 0.57 to 0.71 regression slopes. The  
509 errors likely arise from the relatively low resolution of 500 m close to the shore and limitations  
510 of the spectral model in resolving the transformation of the dominant wave events into the  
511 shadow areas.

#### 512 *4.3 Comparison with Previous Hindcast*

513 The present hindcast utilizes the updated source-term package from Ardhuin et al. (2010) and  
514 the CFSR winds with high-resolution WRF winds around Hawaii. We have already  
515 demonstrated the role of the high-resolution winds in the local wave field. A comparison with  
516 selected previous datasets can infer the added values of the source term package and CFSR.

517 Table 4 compares the error metrics computed for the present dataset and the NOAA NCEP  
518 WAVEWATCH III hindcast of Chawla et al. (2013) at four offshore buoys around Hawaii. The  
519 comparison makes use of available buoy records during the span of the NOAA hindcast from  
520 1979 to 2007. The NOAA hindcast utilized the CFSR wind forcing and the source term package  
521 of Tolman and Chalikov (1996), which is known to underestimate the dissipation and  
522 overestimate the swell energy (Hanson et al., 2009; Stopa et al., 2015). The present hindcast  
523 shows comparable correlation coefficients and scatter indices due to the use of the same wind  
524 forcing. For the comparable offshore resolution, the consistent reduction of the positive bias,  
525 RMSE, and the regression slope point to improvement of the generation and dissipation  
526 mechanisms in the source term of Ardhuin et al. (2010).

527 Table 5 compares the error metrics from the present study with the previous hindcast of  
528 Stopa et al. (2013), which used the source term of Tolman and Chalikov (1996) and the lower  
529 resolution FNL global winds. The high-resolution computations with WRF wind forcing around  
530 the Hawaiian Islands in both studies allow direct comparison of the hindcast datasets at the near-  
531 shore buoys. The error metrics are recomputed at the buoys considered in the earlier hindcast  
532 using available measurements from 2000 to 2009. The present hindcast shows consistent  
533 improvement in terms of the RMSE, correlation coefficient, and scatter index. This is reflected in  
534 the accurate description of the individual events from the CFSR winds as illustrated in the time  
535 series comparison in Figure 11. The two datasets have comparable positive bias at buoys open to  
536 the north Pacific swells despite the lower dissipation in the source term used in the previous  
537 study. Furthermore, the present hindcast has higher linear regression slopes closer to one. This  
538 alludes to the underestimation of the wind forcing from FNL and highlights the improvement of  
539 CFSR in describing the more severe events as pointed out by Stopa and Cheung (2014).

540 The positive bias of the swell prediction is still present with the source term of Ardhuin et al.  
541 (2010) and is a topic of on-going investigation (Stopa et al., 2015). On the other hand, the  
542 present hindcast tends to give negative bias at sheltered locations as shown in Table 3 and Figure  
543 10 despite the overestimation of the approaching swells. This is likely attributed to the absence

544 of diffraction in the governing equation used by the spectral wave models. As part of a  
545 sensitivity study prior to the production, we conducted a series of numerical experiments with  
546 the approximate diffraction scheme in the Oahu SWAN model and did not obtain noticeable  
547 improvement of the results at Buoy 51207 in the shadow of northwest swells. Further  
548 development and calibration of the diffraction scheme is needed to account for the energy  
549 transfer into the sheltered region behind a massive headland or island.

## 550 **5. Conclusions**

551 A system of nested mesoscale atmospheric and spectral wave models driven by the Climate  
552 Forecast System Reanalysis (CFSR) has produced high-resolution regional wind and wave data  
553 from 1979 to 2013. The 34-year dataset provides a wealth of information for climate research,  
554 infrastructure planning, and resources assessment in Hawaii. The use of CFSR and the updated  
555 source term in WAVEWATCH III provides improved description of the ocean waves in  
556 comparison to previous and existing hindcasts. The high-resolution computations capture unique  
557 features of the regional wind and wave fields along the Hawaiian Islands. The multi-modal sea  
558 states include waves generated by trade winds, cold fronts, and Kona storms as well as swells  
559 from north and south Pacific extratropical storms. Comprehensive satellite and buoy  
560 measurements allow validation of the hindcast for practical application and identification of  
561 model limitations for the challenging island environments.

562 The QuikSCAT and buoy measurements from 2000 to 2009 provide assessment of the spatial  
563 and temporary patterns of the regional wind hindcast. The computed wind data captures the year-  
564 round trade winds as well as episodic cold fronts and Kona storms in Hawaii. The persistent  
565 trade winds from the east and northeast dominate the orographically induced airflows that  
566 include deceleration on the windward slopes, acceleration in channels and around southern  
567 Hawaii Island, and prominent wake formation leeward of the islands. Comparison with  
568 QuikSCAT wind fields shows good overall agreement of the seasonal variation of the trade wind  
569 flow as well as its local deceleration and acceleration around the islands. Discrepancies primarily

570 occur in the wake regions leeward of the islands due to inadequate spatial resolution of  
571 QuikSCAT and its overestimation of under calm and variable conditions. The cold fronts and  
572 Kona storms are rapidly varying systems passing through the islands within a period of several  
573 days. Comparison with the measurements shows good reproduction of the general flow patterns  
574 and timing of the events.

575 The wave climate in Hawaii is dominated by trade wind waves and north Pacific swells. The  
576 south swells, despite their year-around occurrence, are typically small and masked by the  
577 dominant wave components. Cold fronts and Kona storms are less frequent, but can generate  
578 severe wave conditions. The altimetry observations provide validation of the spatial patterns of  
579 selected events corresponding to these wave regimes. The long-term comparison of the hindcast  
580 with available buoy measurements from 1979 to 2013 and altimetry measurements from 1991 to  
581 2011 primarily reflects the dominant trade wind waves and north Pacific swells. The hindcast  
582 provides a good description of the trade wind waves but tends to overestimate the energetic  
583 northwest swell. The spectral models, however, underestimate the wave height in the shadows of  
584 both the wind waves and swells. Accurate modeling of the wave fields at sheltered locations  
585 requires diffraction and other energy transfer mechanisms in the model. The comparison with the  
586 recorded data validates the 34-year hindcast dataset and identifies limitations of spectral wave  
587 modeling for island environments. In addition to climate research and engineering application,  
588 the hindcast dataset provides a baseline for future model development and parameterization  
589 especially for island environments.

## 590 **Acknowledgements**

591 The Department of Energy is the primary sponsor for the development of the hindcast dataset  
592 with funding through Grant No. DE-FG36-08G018180 via the Hawaii National Marine  
593 Renewable Energy Center. The Department of Navy provided additional support through Task  
594 Order No. N00024-08-D-6323 via Applied Research Laboratory at the University of Hawaii.  
595 SOEST Contribution Number XXXX.

596 **References**

- 597 Arduin, F., Rogers, E., Babanin, A., Filipot, J.-F., Magne, R., Roland, A., van der Westhuysen,  
598 A., Queffelec, P., Lefevre, J.-M., Aouf, L., Collard, F., 2010. Semi-empirical dissipation source  
599 functions for ocean waves. Part I: Definition, calibration, and validation. *Journal of Physical*  
600 *Oceanography*, 40(9), 1917–1941.
- 601 Arinaga, R.A., Cheung, K.F., 2012. Atlas of global wave energy from 10 years of reanalysis and  
602 hindcast data. *Renewable Energy*, 39 (1), 49–64.
- 603 Aucan, J.P., 2006. Directional wave climatology for the Hawaiian Islands from buoy data and  
604 the influence of ENSO on extreme wave events from wave model hindcast. *Proceedings of the*  
605 *9th International Workshop on Wave Hindcasting and Forecasting*, Victoria, British Columbia.
- 606 Banner, M.L., Morison, R.P., 2010. Refined source terms in wind wave models with explicit  
607 wave breaking prediction. Part I: Assessment of existing model performance. *Ocean Modelling*,  
608 33(1-2), 177-189.
- 609 Bidlot, J., Janssen, P., Abdalla, S., 2007. A revised formulation for ocean wave dissipation and  
610 its model impact. *ECMWF Technical Memorandum 509*, Reading, UK.
- 611 Boisséson, E., Balmaseda, M. A., Abdalla, S., Källén, E., Janssen, P. A. E. M., 2014. How robust  
612 is the recent strengthening of the Tropical Pacific trade winds? *Geophysical Research*  
613 *Letters*, 41(12), 4398-4405.
- 614 Booij, N., Ris, R.C., Holthuijsen, L.H., 1999. A third-generation wave model for coastal regions,  
615 Part I, Model description and validation. *Journal of Geophysical Research*, 104(C4), 7649-7666.
- 616 Caires, S., Sterl, A., Bidlot, J.-R., Graham, N., Swail, V., 2004. Intercomparison of different  
617 wind-wave reanalysis. *Journal of Climate*, 17(10), 1893-1913.
- 618 Caldwell, P.C., Vitousek, S., Aucan, J.P., 2009. Frequency and duration of coinciding high surf  
619 and tides along the north shore of Oahu, Hawaii. *Journal of Coastal Research*, 25(3), 734-743.
- 620 Carlis, D.L., Chen, Y.-L., Morris, V.R., 2010. Numerical simulations of island-scale airflow over  
621 Maui and the Maui vortex during summer trade-wind conditions. *Monthly Weather*  
622 *Review*, 138(7), 2706-2736.
- 623 Caruso, S.J., Businger, S., 2006. Subtropical Cyclogenesis over the central north Pacific.  
624 *Weather and Forecasting*, 21 (2), 193-205.
- 625 Cheung, K.F., Bai, Y., Yamazaki, Y., 2013. Surges around the Hawaiian Islands from the 2011  
626 Tohoku tsunami. *Journal of Geophysical Research: Oceans*, 118(10), 5703-5719.
- 627 Dee, D.P., Uppala, S.M., Simmons, A.J., Berrisford, P., Poli, P., Kobayashi, S., Andrae, U.,  
628 Balmaseda, M.A., Balsamo, G., Bauer, P., Bechtold, P., Beljaars, A.C.M., van der Berg, L.,  
629 Bidlot, J., Bormann, N., Delsol, C., Dragani, R., Fuentes, M., Geer, A. J., Haimberger, L., Healy,

630 S. B., Hersbach, H., Hólm, E. V., Isaksen, L., Kållberg, P., Köhler, M., Matricardi, M., McNally,  
631 A. P., Monge-Sanz, B. M., Morcrette, J.-J., Park, B.-K., Peubey, C., de Rosnay, P., Tavalato, C.,  
632 Thépaut, J.-N., Vitart, F., 2011. The ERA-Interim reanalysis: configuration and performance of  
633 the data assimilation system. *Quarterly Journal of the Royal Meteorological Society*,  
634 137(656), 553–597.

635 Ebuchi, N., Graber, H.C., Caruso, M.J., 2002. Evaluation of wind vectors observed by  
636 QuikSCAT/SeaWinds using ocean buoy data. *Journal of Atmospheric and Oceanic Technology*,  
637 19(12), 2049-2062.

638 Ek, M. B., Mitchell, K. E., Lin, Y., Rogers, E., Grunmann, P., Koren, V., Gayno, G., Tarpley, J.  
639 D., 2003. Implementation of Noah land surface model advances in the National Centers for  
640 Environmental Prediction operational mesoscale Eta model. *Journal of Geophysical Research:*  
641 *Atmospheres* (1984–2012), 108(D22), DOI: 10.1029/2002JD003296.

642 Filipot, J.-F., Cheung, K.F., 2012. Spectral wave modeling for fringing reef environment. *Coastal*  
643 *Engineering*, 67, 67-79.

644 Foster, J., Li, N., Cheung, K. F., 2014. Sea state determination from ship-based geodetic GPS.  
645 *Journal of Atmospheric and Oceanic Technology*, 31(11), 2556-2564.

646 Fyfe, J.C., 2003. Extratropical southern hemisphere cyclones: harbingers of climate change?  
647 *Journal of Climate*, 16(17), 2802–2805.

648 Garza, J.A., Chu, P.S., Norton, C.W., Schroeder, T.A., 2012. Changes of the prevailing trade  
649 winds over the islands of Hawaii and the North Pacific. *Journal of Geophysical Research:*  
650 *Atmospheres* (1984–2012), 117(D11), DOI: 10.1029/2011JD016888.

651 Griffies, S.M., Harrison, M.J., Pacanowski, R.C., Rosati, A., 2004. Technical Guide to MOM4.  
652 GFDL Ocean Group Technical Report No. 5, Princeton, New Jersey, 337 pp.

653 Hanson, J.L., Tracy, B.A., Tolman, H.L., Scott, R.D., 2009. Pacific hindcast performance of  
654 three numerical wave models. *Journal of Atmospheric and Oceanic Technology*, 26(8), 1614-  
655 1633.

656 Hitzl, D.E., Chen, Y.-L., Nguyen, H.V., 2014. Numerical simulations and observations of  
657 airflow through the 'Alenuihaha Channel, Hawaii. *Monthly Weather Review*, 142(12), 4696-  
658 4718.

659 JPL, 2000. QuikSCAT Science Data Product User's Manual. Jet Propulsion Laboratory  
660 Publication D-18053, Pasadena, California, 84 pp.

661 Leckler, F., Ardhuin, F., Filipot, J.-F., Mironov, A., 2013. Dissipation source terms and whitecap  
662 statistics. *Ocean Modelling*, 70(9), 62-74.

663 Li, N., Roeber, V., Yamazaki, Y., Heitmann, T. W., Bai, Y., Cheung, K. F., 2014. Integration of  
664 coastal inundation modeling from storm tides to individual waves. *Ocean Modelling*, 83, 26-42.

- 665 McPhaden, M.J., Zebiak, S.E., Glantz, M.H., 2006. ENSO as an integrating concept in earth  
666 science. *Science*, 314(5806), 1740-1745.
- 667 Nguyen, H. V., Chen, Y.-L., Fujioka, F., 2010. Numerical simulations of island effects on  
668 airflow and weather during the summer over the Island of Oahu. *Monthly Weather*  
669 *Review*, 138(6), 2253–2280.
- 670 O'Connor, C.F., Chu, P.S., Hsu, P.C., Kodama, K., 2015. Variability of Hawaiian winter rainfall  
671 during La Niña events since 1956. *Journal of Climate*, 28 (19), 7809-7823.
- 672 Otkin, J.A., Martin, J.E., 2004. A synoptic climatology of the subtropical Kona Storm. *Monthly*  
673 *Weather Review*, 132(6), 1502–1517.
- 674 Pensieri, S., Bozzano, R., Schiano, M.E., 2010. Comparison between QuikSCAT and buoy wind  
675 data in the Ligurian Sea. *Journal of Marine Systems*, 81(4), 286-296.
- 676 Ponce de Leon, S., Guedes Soares, C., 2005. On the sheltering effects of islands in ocean wave  
677 models. *Journal of Geophysical Research - Ocean*, 110 (C9), 2156-2202.
- 678 Queffeuou, P., Croizé-Fillon, D., 2010. Global Altimeter SWH Data Set, Version 7. May 2010  
679 Technical Report, Ifremer, France.  
680 (<ftp://ftp.fremer.fr/ifremer/cersat/products/swath/altimeters/waves/documentation/altimeterwave>  
681 [merge7.0.pdf](ftp://ftp.fremer.fr/ifremer/cersat/products/swath/altimeters/waves/documentation/altimeterwave).)
- 682 Rasclé, N., Ardhuin, F., 2013. A global wave parameter database for geophysical applications.  
683 Part 2: Model validation with improved source term parameterization. *Ocean Modelling*, 70,  
684 174-188.
- 685 Rogers, W.E., Babanin, A.V., Wang, D.W., 2012. Observation-consistent input and  
686 whitecapping dissipation in a model for wind-generated surface waves: description and simple  
687 calculations. *Journal of Atmospheric and Oceanic Technology*, 29(9), 1329-1346.
- 688 Saha, S., Moorthi, S., Pan, H.L., Wu, X., Wang, J., Nadiga, S., Tripp, P., Kistler, R., Woolen, J.,  
689 Behringer, D., Liu, H., Stokes, D., Grumbine, R., Gayno, G., Wang, J., Hou, Y.T., Chuang, H.,  
690 Juang, H.M.J., Sela, J., Irdell, M., Treadon, R., Klesits, D., Felst, P.V., Keyser, D., Derber, J., Ek,  
691 M., Meng, J., Wei, H., Yang, R., Lord, S., van den Dool, H., Kumar, A., Wang, W., Long, C.,  
692 Chelliah, M., Xue, Y., Huang, B., Schemm, J., Ebisuzaki, W., Lin, R., Xie, P.P., Chen, M., Zhou,  
693 S., Higgins, W., Zou, C.Z., Liu, Q., Chen, Y., Han, Y., Cucurull, L., Reynolds, R.W., Rutledge,  
694 G., Goldberg, M., 2010. The NCEP climate forecast system reanalysis. *Bulletin of the American*  
695 *Meteorological Society*, 91(7), 1015–1057.
- 696 Saha, S., Moorthi, S., Wu, X., Wang, J., Nadiga, S., Tripp, P., Behringer, D., Hou, Y.T., Chuang,  
697 H., Irdell, M., Ek, M., Meng, J., Yang, R., Mendez, M.P., Dool, H., Zhang, Q., Wang, W., Chen,  
698 M., Becker, E., 2014. The NCEP climate forecast system version 2. *Journal of Climate*, 27(6),  
699 2185–2208.

700 Satheesan, K., Sarkar, A., Parekh, A., RameshKumar, M.R., Kuroda, Y., 2007. Comparison of  
701 wind data from QuikSCAT and buoys in the Indian Ocean. *International Journal of Remote*  
702 *Sensing*, 28(10), 2375–2382.

703 Simpson, R.H., 1952. Evolution of the Kona storm a subtropical cyclone. *Journal of*  
704 *Meteorology*, 9(1), 24–35.

705 Skamarock, W.C., Klemp, J.B., 2008. A time-split nonhydrostatic atmospheric model for  
706 weather and forecasting applications. *Journal of Computational Physics*, 227(7), 3465-3485.

707 Stopa, J.E., Ardhuin, F., Babanin, A.V., Zieger, S., 2015. Comparison and validation of physical  
708 wave parameterizations in spectral wave models. *Ocean Modelling*, Special Issue on Surface  
709 Waves doi: 10.1016/j.ocemod.2015.09.003.

710 Stopa, J.E., Cheung, K.F., 2014. Periodicity and patterns of ocean wind and wave climate.  
711 *Journal of Geophysical Research: Oceans*, 119(8), 5563-5584.

712 Stopa, J. E., Cheung, K. F., Chen, Y.-L., 2011. Assessment of wave energy resources in Hawaii.  
713 *Renewable Energy*, 36(2), 554-567.

714 Stopa, J.E., Filipot, J.-F., Li, N., Cheung, K.F., Chen, Y.-L., and Vega, L., 2013. Wave energy  
715 resources along the Hawaiian Islands chain. *Renewable Energy*, 55, 305-321.

716 Stopa, J.E., Cheung, K.F., Tolman, H.L., Chawla, A., 2013. Patterns and cycles in the climate  
717 forecast system reanalysis wind and wave data. *Ocean Modelling*, 70, 207–220.

718 Stopa, J.E., Cheung, K.F., 2014. Intercomparison of wind and wave data from the ECMWF  
719 Reanalysis Interim and NCEP Climate Forecast System Reanalysis. *Ocean Modelling*, 75, 65-83.

720 Tu, C.-C., Chen, Y.-L., 2011. Favorable conditions for the development of a heavy rainfall event  
721 over Oahu during the 2006 wet period. *Weather Forecasting* , 26(3), 280-300.

722 Tolman, H. L., 2008. A mosaic approach to wind wave modeling. *Ocean Modelling*, 25, 35-47.

723 Tolman, H.L., Banner, M.L., Kaihatu, J.M., 2013. The NOPP operational wave model  
724 improvement project. *Ocean Modelling*, 70, 2-10.

725 Tolman, H.L., Chalikov, D., 1996. Source terms in a third-generation wind wave model. *Journal*  
726 *of Physical Oceanography*, 26(2), 2497–2518.

727 Tolman, H.L., and the WAVEWATCH III ® Development Group. 2014. User Manual and  
728 System Documentation of WAVEWATCH III® version 4.18. Technical Note 316,  
729 NOAA/NWS/ NCEP/MMAB, 282 pp. + Appendices.

730 Van der Westhuysen, A.J., 2007. Advances in the Spectral Modelling of Wind waves in the  
731 Nearshore. Ph.D. thesis, Delft University of Technology, the Netherlands.

- 732 Van der Westhuysen, A.J., Zijlema, M., Battjes, J.A., 2007. Nonlinear saturation based  
733 whitecapping dissipation in SWAN for deep and shallow water, *Coastal Engineering*, 54(2), 151-  
734 170.
- 735 Yang, F., Pan, H.L., Krueger, S.K., Moorthi, S., Lord, S.J., 2006. Evaluation of the NCEP Global  
736 Forecast System at the ARM SGP site. *Monthly Weather Review*, 134(12), 3668-3690.
- 737 Yang, Y., Chen, Y.-L., Fujioka, F. M., 2005. Numerical simulations of the island-induced  
738 circulation over the island of Hawaii during HaRP. *Monthly Weather Review*, 133(12), 3693-  
739 3713.
- 740 Yin, J.H., 2005. A consistent poleward shift of the storm tracks in simulations of 21st century  
741 climate. *Geophysical Research Letters*, 32(18), DOI:10.1029/2005GL023684.
- 742 Young, I.R., Zieger, S., Babanin, A.V., 2011. Global trends in wind speed and wave height.  
743 *Science*, 332(6028), 451-455.
- 744 Zhang, Y., Chen, Y.-L., Schroeder, T.A., Kodama, K., 2005. Numerical simulations of sea  
745 breeze circulations over northwest Hawaii. *Weather and Forecasting*, 20(6), 827-846.
- 746 Zhou, C, Chen, Y.-L., 2014. Assimilation of GPS RO refractivity data and its impact on  
747 simulations of trade wind inversion and a winter cold front in Hawaii. *Natural Science*, 6(8),  
748 605-614.
- 749 Zieger, S., Babanin, A.V., Rogers, W. E., Young, I. R., 2015. Observation-based source terms in  
750 the third-generation wave model WAVEWATCH. *Ocean Modelling*, 96(1), 2-25.
- 751 Zieger, S., Vinoth, J., Young, I.R., 2009. Joint calibration of multi-platform altimeter  
752 measurements of wind Speed and wave Height over the past 20 Years. *Journal of Atmospheric  
753 and Oceanic Technology*, 26(12), 2549-2564.

754 **List of Figures**

- 755 1. Illustration of Hawaii wave climate, location map for buoys and geographical features, and  
756 layout of nested computational grids for WAVEWATCH III and SWAN.
- 757 2. Meteorological and wave conditions from models and satellites for the trade wind event on  
758 August 17, 2005. The red and black boxes in the left panels outline the high-resolution WRF and  
759 WATCHWATCH III domains.
- 760 3. Meteorological and wave conditions from models and satellites for the cold front on March 1,  
761 2004. The red and black boxes in the left panels outline the high-resolution WRF and  
762 WATCHWATCH III domains.
- 763 4. Meteorological and wave conditions from models and satellites for the Kona storm on Dec 5,  
764 2007. The red and black boxes in the left panels outline the high-resolution WRF and  
765 WATCHWATCH III domains.
- 766 5. Wave conditions from models and satellites for the south swell on July 12, 2001.
- 767 6. Wave conditions from models and satellites for the north swell on January 5, 2001.
- 768 7. Mean summer and winter 10-m winds from Hawaii WRF and QuikSCAT for 2000 to 2009.
- 769 8. Error metrics of wind speeds from Hawaii WRF and QuikSCAT for 2000 to 2009.
- 770 9. GlobWAVE altimetry observations around Hawaii from 1991 to 2011. (a) Track distribution.  
771 (b) Number of observations per cell.
- 772 10. Error metrics of significant wave heights from Hawaii WAVEWATCH III and GlobWAVE  
773 altimetry measurements for 1991 to 2011.
- 774 11. Comparison of recorded (black) and hindcast (red) wave parameters at selected offshore and  
775 nearshore buoys for 2012.
- 776 12. Scatter plots of hindcast significant wave heights and buoy measurements at selected  
777 offshore and nearshore buoys. Black line denotes perfect match, blue lines delineate 90% of the  
778 data, and red line is the linear regression
- 779 13. Quantile-quantile plots of hindcast significant wave heights and buoy measurements at  
780 selected offshore and nearshore buoys. Black line denotes perfect match and black dash lines  
781 delineate the  $\pm 5\%$  error bounds.  
782

783 Table 1. Nested computational grids for spectral wave and mesoscale atmospheric modeling.

Model	Grid	Longitude	Latitude	Resolution
WAVEWATCH III	global	180°W-180°E	77.5°S-77.5°N	0.5 arc-degree
WAVEWATCH III	Hawaii	161°W -154°W	18°N-23°N	3 arc-minute
SWAN	Kauai	160.35°W-159.2°W	21.7°N-22.35°N	0.3 arc-minute
SWAN	Maui	157.4°W-155.9°W	20.4°N-21.3°N	0.3 arc-minute
SWAN	Oahu	158.35°W-157.6°W	21.2°N -21.75°N	0.3 arc-minute
SWAN	Hawaii Island	156.2°W-154.7°W	18.85°N-20.35°N	0.3 arc-minute
WRF	Central Pacific	175.67°W ~136.26°W	6.35°N~ 37.98°N	18 km
WRF	Hawaii	167.22°W~ 149.30°W	15.39°N ~ 26.69°N	6 km

784

785 Table 2. Locations and temporal coverage of offshore and nearshore buoys used in model  
786 validation.

Buoy	Computational Grid	Latitude (°N)	Longitude (°W)	Depth (m)	Temporal Coverage
51000	Global WAVEWATCH III	23.546	154.056	4275	2009.4-2013.3
51001	Global WAVEWATCH III	23.445	162.279	3430	1981.2-2009.12
51002	Global WAVEWATCH III	17.094	157.808	5002	1984.9-2013.1
51003	Hawaii WAVEWATCH III	19.018	160.582	4919	1984.11-2013.6
51004	Global WAVEWATCH III	17.602	152.395	5230	1984.11-2013.6
51100	Global WAVEWATCH III	23.558	153.900	4755	2009.4-2013.6
51101	Global WAVEWATCH III	24.321	162.058	4792	2008.2-2013.6
51201	Oahu SWAN	21.669	158.120	200	2001.12-2013.6
51202	Oahu SWAN	21.414	157.679	82	2000.8-2013.6
51204	Oahu SWAN	21.281	158.124	302	2010.10-2013.6
51207	Oahu SWAN	21.4775	157.7526	81	2012.10-2013.6
KNOH1	Oahu SWAN	21.288	157.865	12	2008.9-2012.1
39	Kauai SWAN	22.00667	159.8333	110	1982.10-1993.9
51203	Maui SWAN	20.78778	157.0098	201	2007.5-2013.6
51205	Maui SWAN	21.0195	156.4272	193	2011.12-2013.6
51206	Hawaii Island SWAN	19.78143	154.968	347	2012.3-Present

787

788

Table 3. Error metrics of significant wave height at buoys.

Buoy	Start Time	End Time	Error bounds* ( $\pm$ m)	ME (m)	RMSE (m)	COR	SI	Lin. Reg. slop
51000	04/23/2009	03/10/2013	0.69	0.27	0.46	0.89	0.16	0.96
51001	02/11/1981	12/24/2009	0.63	0.14	0.44	0.90	0.17	0.95
51002	09/06/1984	01/14/2013	0.61	0.16	0.41	0.85	0.16	0.94
51003	11/01/1984	05/31/2013	0.57	0.10	0.41	0.83	0.18	0.92
51004	11/08/1984	05/31/2013	0.44	0.06	0.29	0.89	0.12	0.87
51100	04/23/2009	05/31/2013	0.65	0.28	0.45	0.90	0.16	0.99
51101	02/21/2008	05/31/2013	0.68	0.28	0.47	0.91	0.17	0.99
51201	09/08/2004	05/31/2013	0.52	0.18	0.35	0.91	0.19	0.96
51202	09/08/2004	05/31/2013	0.35	0.01	0.22	0.92	0.12	0.90
51204	10/13/2010	05/31/2013	0.37	-0.06	0.23	0.78	0.17	0.65
51207	10/29/2012	05/31/2013	0.34	0.02	0.21	0.94	0.12	0.92
KNOH1	09/01/2008	01/18/2012	0.27	-0.07	0.18	0.67	0.23	0.57
39	10/22/1982	09/16/1993	0.90	0.37	0.60	0.87	0.28	1.01
51203	07/01/2007	05/31/2013	0.35	-0.12	0.22	0.71	0.20	0.71
51205	12/05/2011	05/31/2013	0.60	0.21	0.37	0.89	0.15	0.98
51206	03/05/2012	05/31/2013	0.41	-0.01	0.25	0.89	0.12	0.82

789 \* Error bounds for 90% of the hindcast data from the measurements as illustrated in Figure 12.

790 Table 4. Error metrics of significant wave height from the present and NOAA NCEP hindcasts.

Buoy	Start Time	End Time	ME (m)		RMSE (m)		COR		SI		Lin. Reg. slop	
			NOAA	Present	NOAA	Present	NOAA	Present	NOAA	Present	NOAA	Present
51001	02/11/1981	12/31/2007	0.24	0.14	0.49	0.44	0.91	0.90	0.18	0.17	1.05	0.95
51002	09/06/1984	12/31/2007	0.21	0.14	0.45	0.40	0.86	0.85	0.16	0.16	1.04	0.94
51003	11/01/1984	12/31/2007	0.13	0.07	0.42	0.39	0.86	0.85	0.18	0.17	1.07	0.96
51004	11/08/1984	12/31/2007	0.15	0.04	0.34	0.29	0.89	0.89	0.13	0.12	0.99	0.87

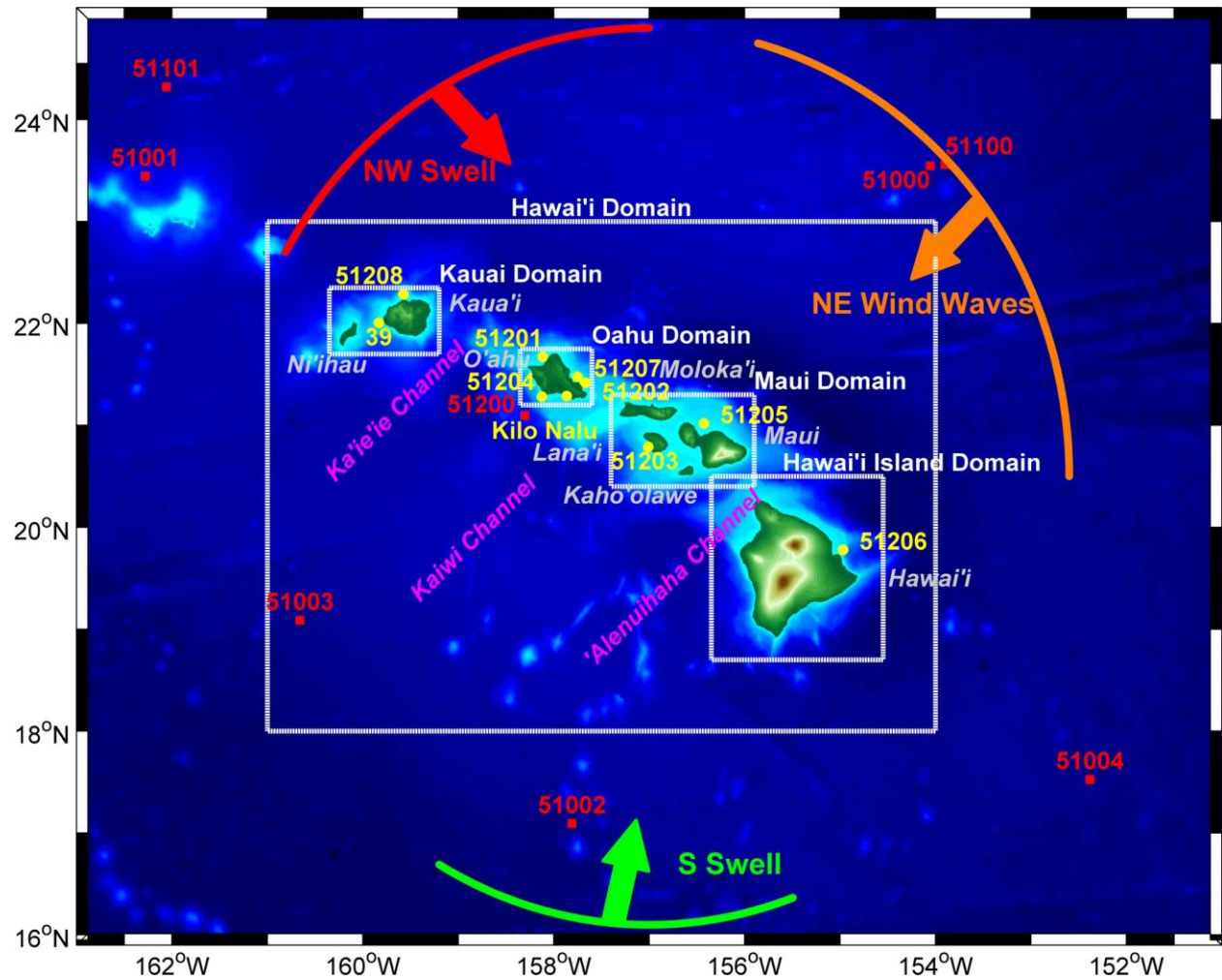
791

792

793 Table 5. Error metrics of significant wave height from the present hindcast and the prior work of  
 794 Stopa et al. (2013).

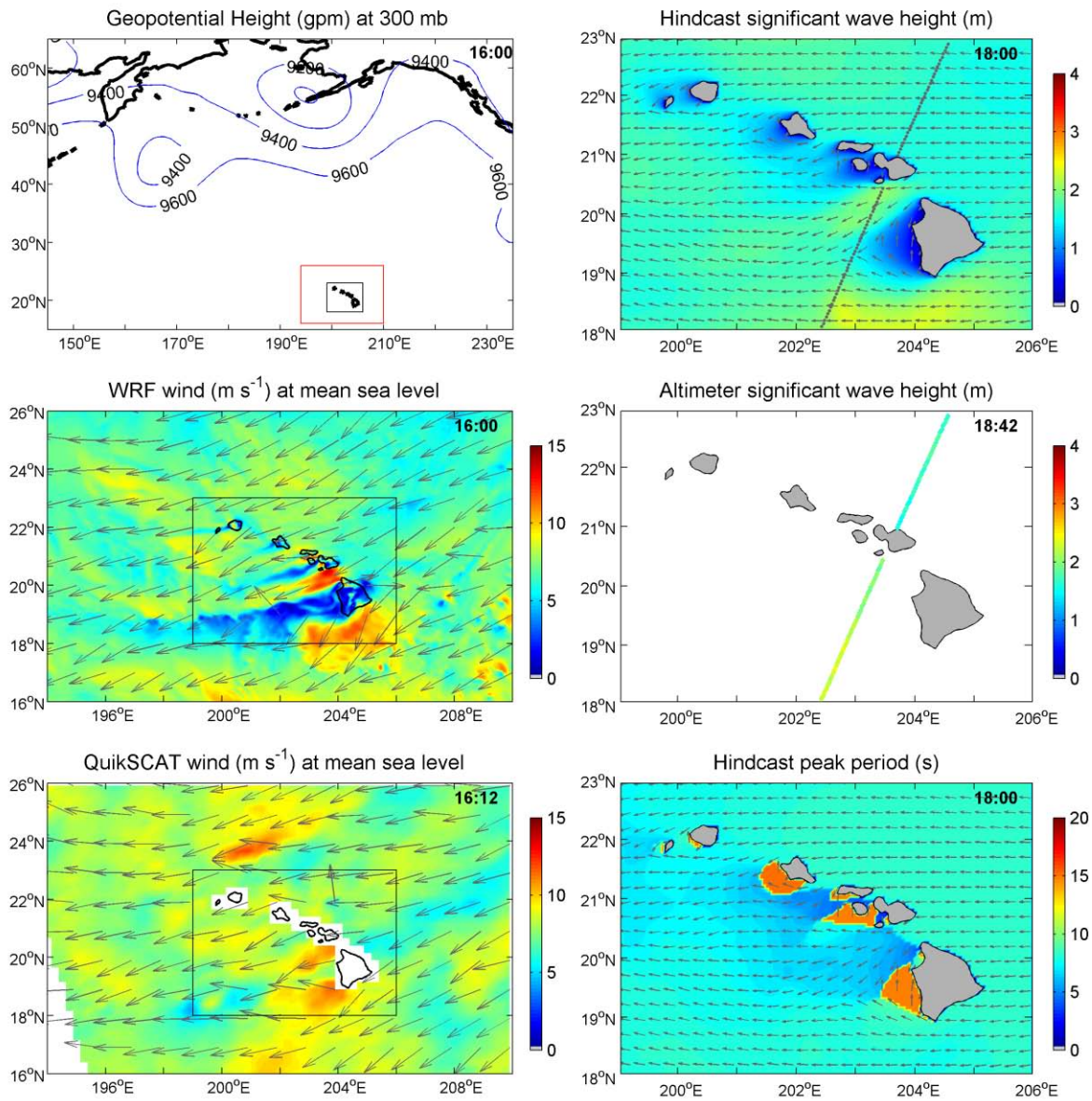
Buoy	Start Time	End Time	ME (m)		RMSE (m)		COR		SI		Lin. Reg. slop	
			Prior	Present	Prior	Present	Prior	Present	Prior	Present	Prior	Present
51001	01/02/2000	12/24/2009	0.08	0.14	0.38	0.39	0.90	0.91	0.16	0.16	0.83	0.95
51002	01/02/2000	12/31/2009	0.11	0.16	0.39	0.36	0.80	0.87	0.15	0.14	0.81	0.93
51003	01/02/2000	12/31/2009	0.1	0.06	0.38	0.33	0.81	0.86	0.17	0.15	0.82	0.93
51004	01/02/2000	10/07/2009	0.02	0.06	0.29	0.24	0.87	0.91	0.12	0.10	0.75	0.85
51100	04/24/2009	12/31/2009	0.26	0.20	0.44	0.35	0.89	0.92	0.16	0.14	0.88	0.90
51101	02/21/2008	12/31/2009	0.26	0.24	0.49	0.46	0.88	0.90	0.19	0.18	0.82	0.93
51201	09/08/2004	12/31/2009	0.09	0.17	0.35	0.35	0.90	0.92	0.2	0.19	0.92	0.96
51202	09/08/2004	12/30/2009	0.09	-0.01	0.29	0.23	0.89	0.92	0.14	0.12	0.86	0.88
51203	07/01/2007	12/31/2009	0.11	-0.13	0.26	0.22	0.67	0.76	0.27	0.20	0.70	0.73
KNOH1	09/01/2008	12/31/2009	0.09	-0.07	0.23	0.18	0.59	0.68	0.28	0.23	0.60	0.56

795  
 796

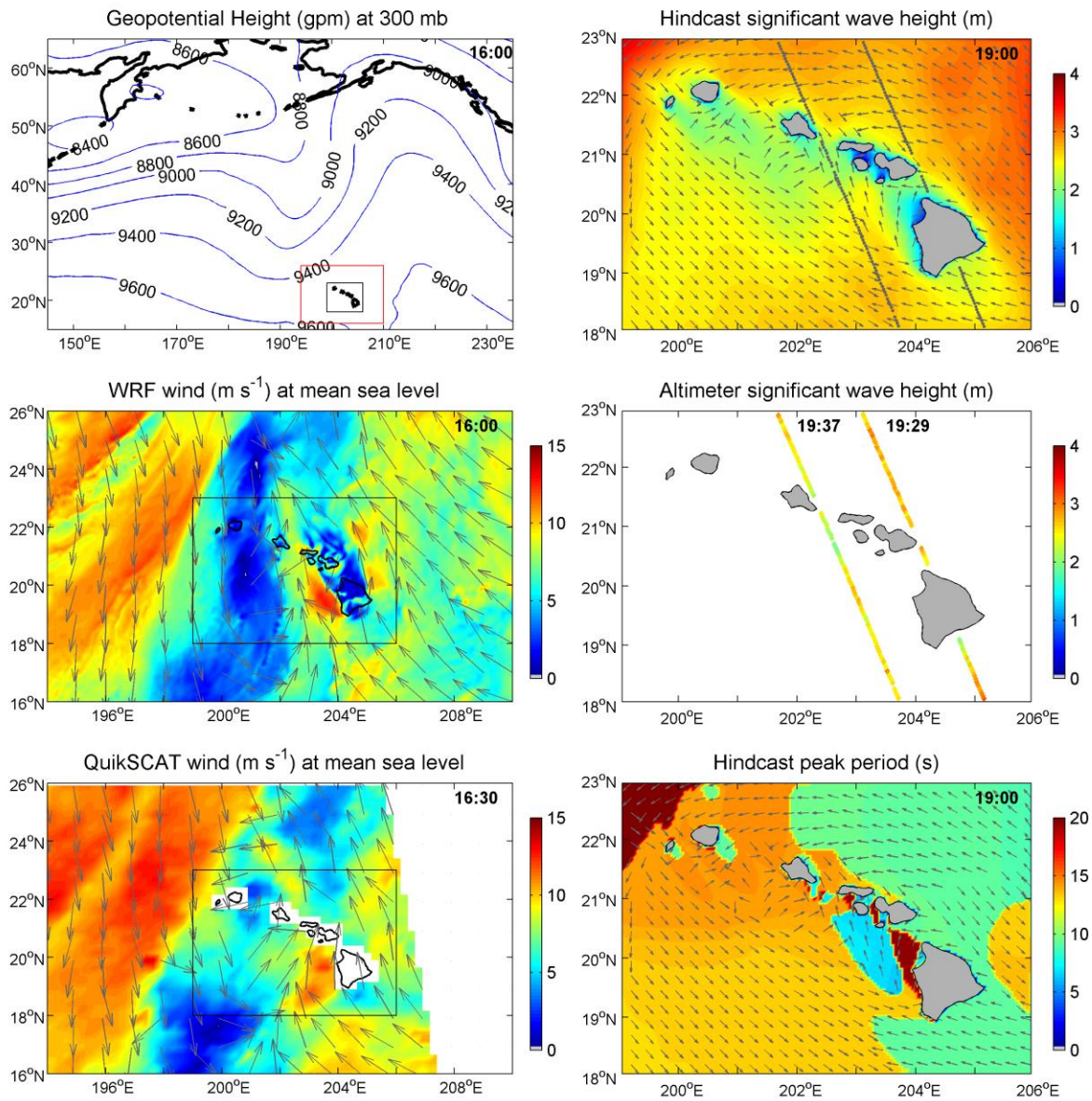


797  
798  
799  
800  
801

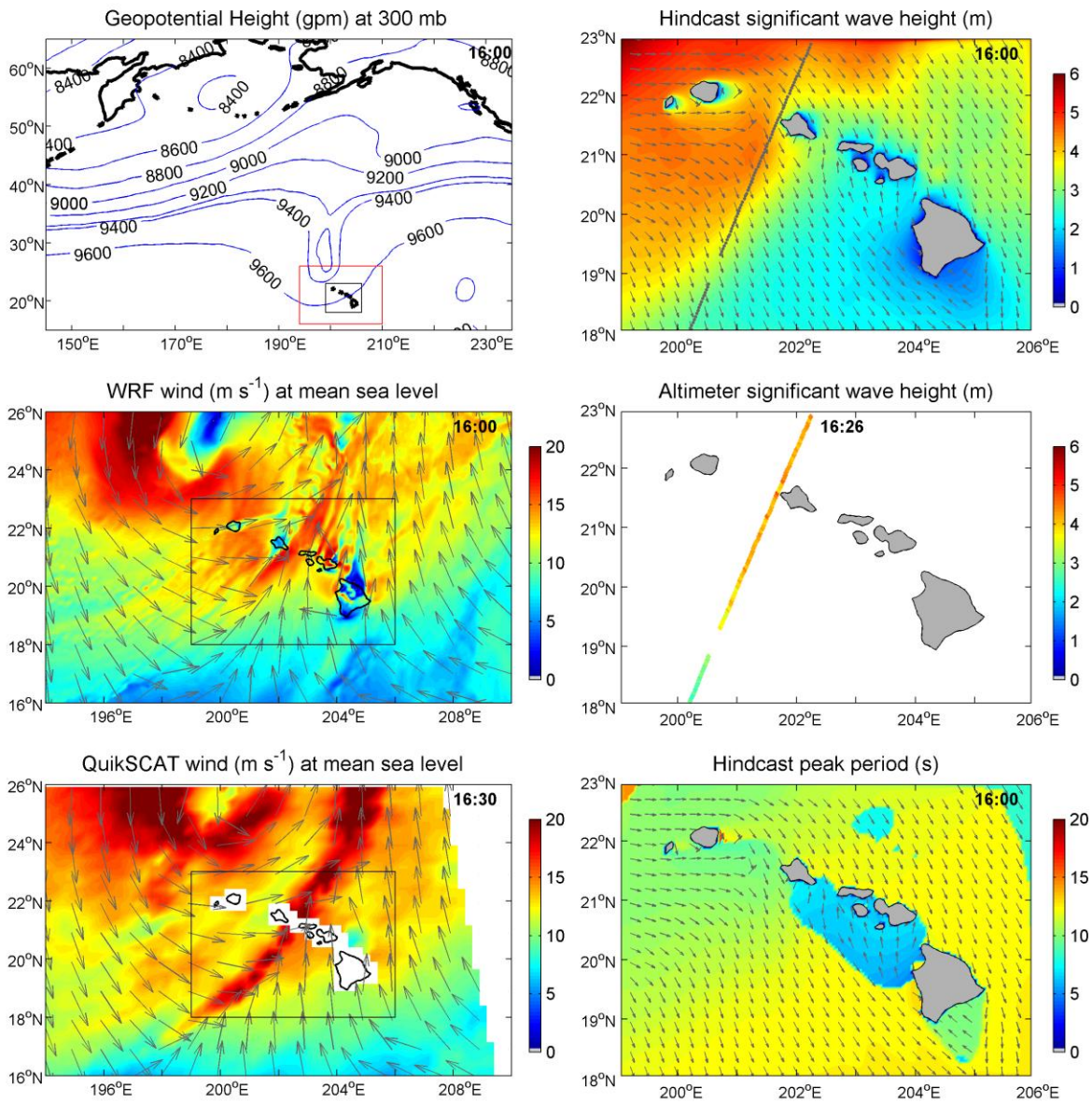
Figure 1. Illustration of Hawaii wave climate, location map for buoys and geographical features, and layout of nested computational grids for WAVEWATCH III and SWAN.



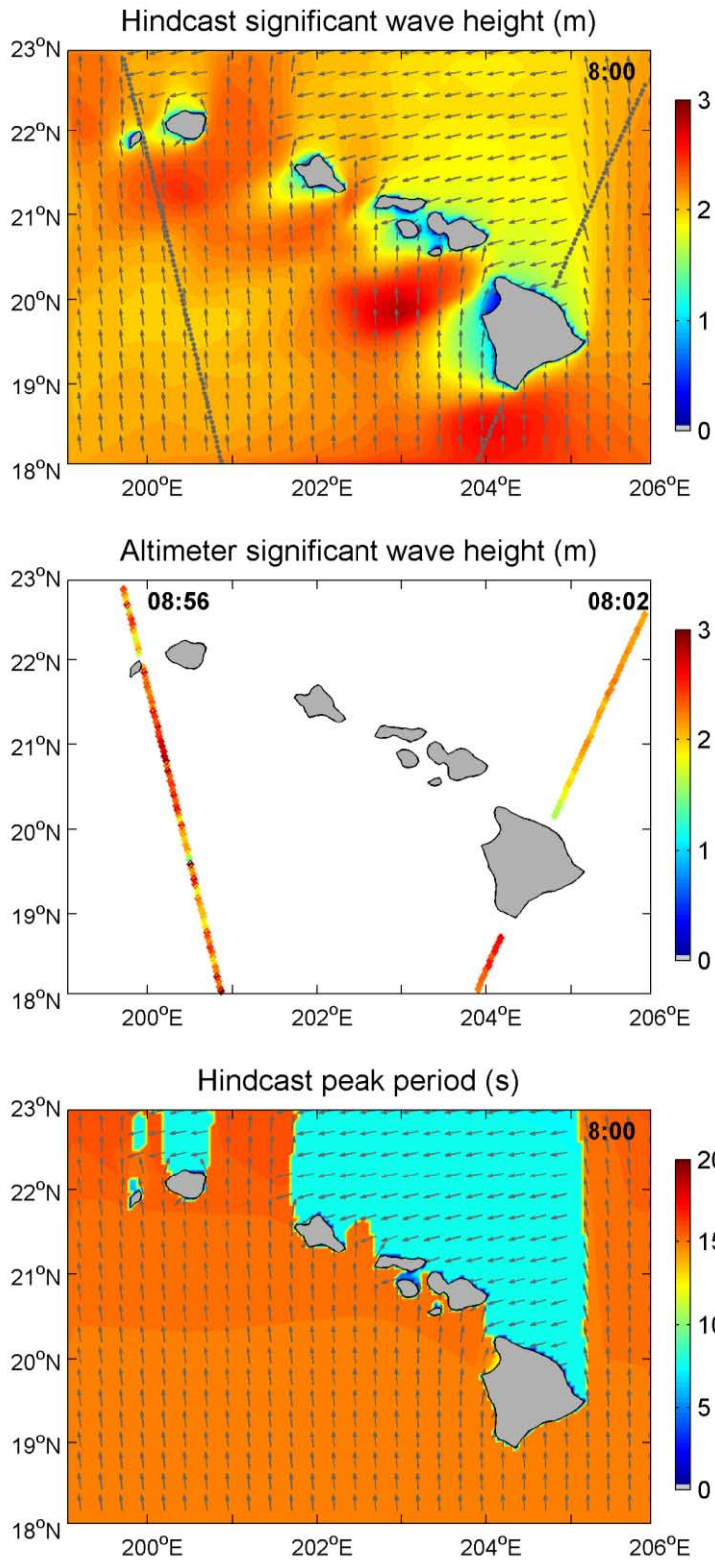
802  
 803 Figure 2. Meteorological and wave conditions from models and satellites for the trade wind  
 804 event on August 17, 2005. The red and black boxes in the left panels outline the high-resolution  
 805 WRF and WATCHWATCH III domains.  
 806



807  
 808 Figure 3. Meteorological and wave conditions from models and satellites for the cold front on  
 809 March 1, 2004. The red and black boxes in the left panels outline the high-resolution WRF and  
 810 WATCHWATCH III domains.  
 811



812  
 813 Figure 4. Meteorological and wave conditions from models and satellites for the Kona storm on  
 814 Dec 5, 2007. The red and black boxes in the left panels outline the high-resolution WRF and  
 815 WATCHWATCH III domains.  
 816

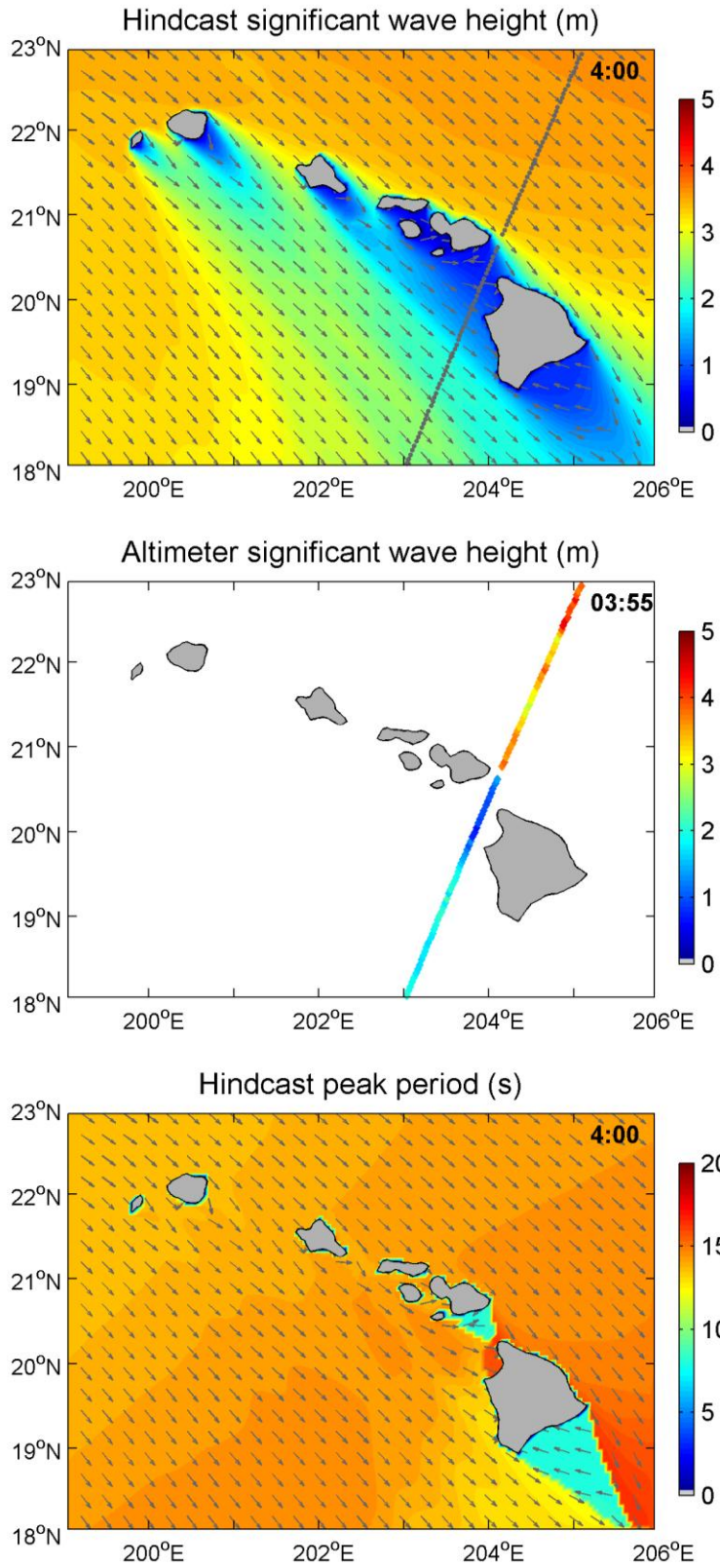


817

818 Figure 5. Wave conditions from models and satellites for the south swell on July 12, 2001.

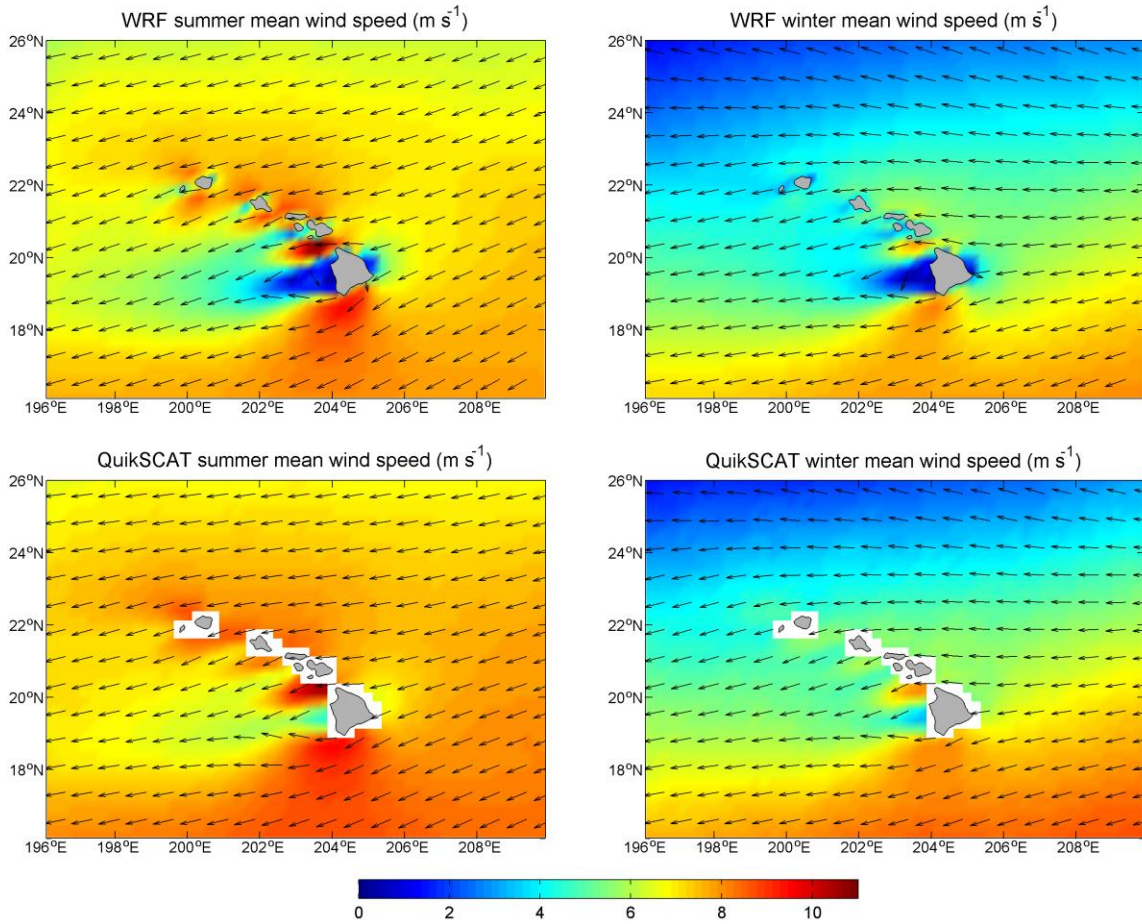
819

820



821  
822  
823

Figure 6. Wave conditions from models and satellites for the north swell on January 5, 2001.

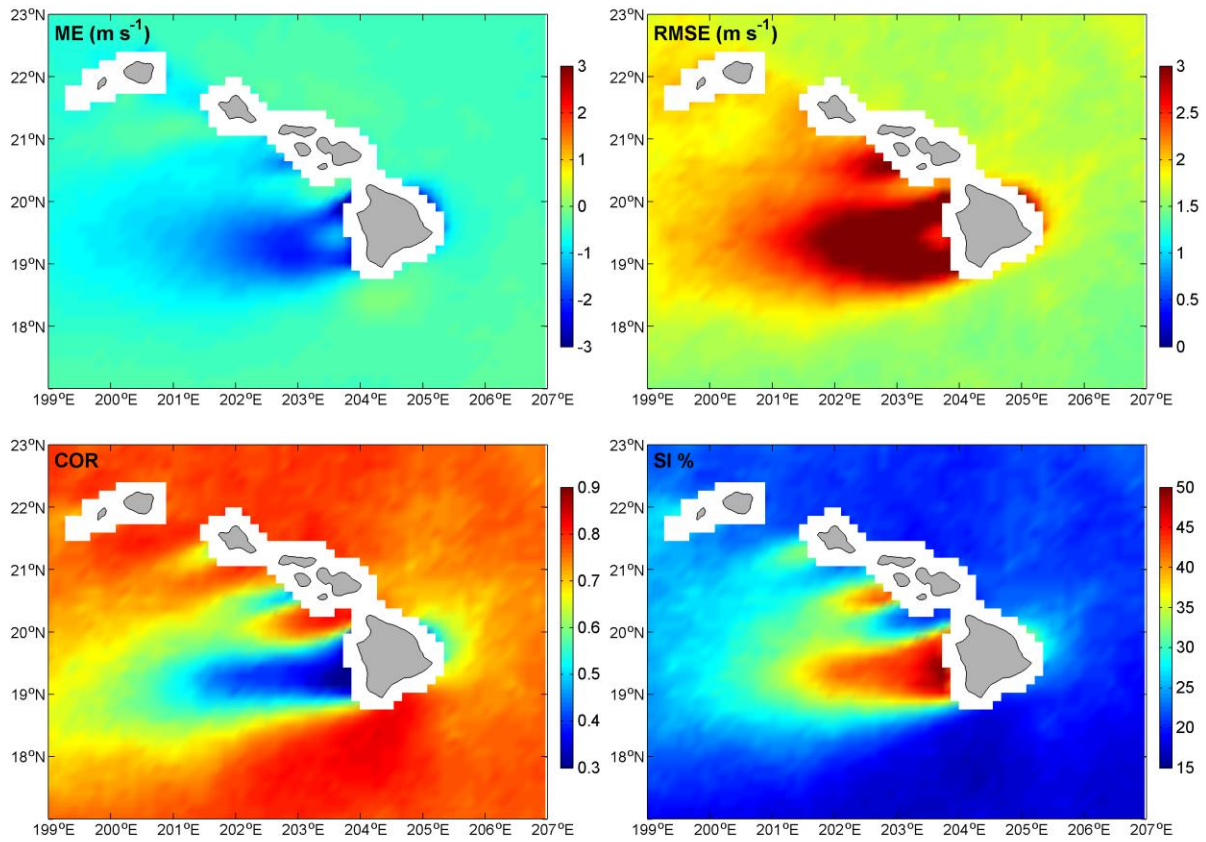


824

825 Figure 7. Mean summer and winter 10-m winds from Hawaii WRF and QuikSCAT for 2000 to  
 826 2009.

827

828

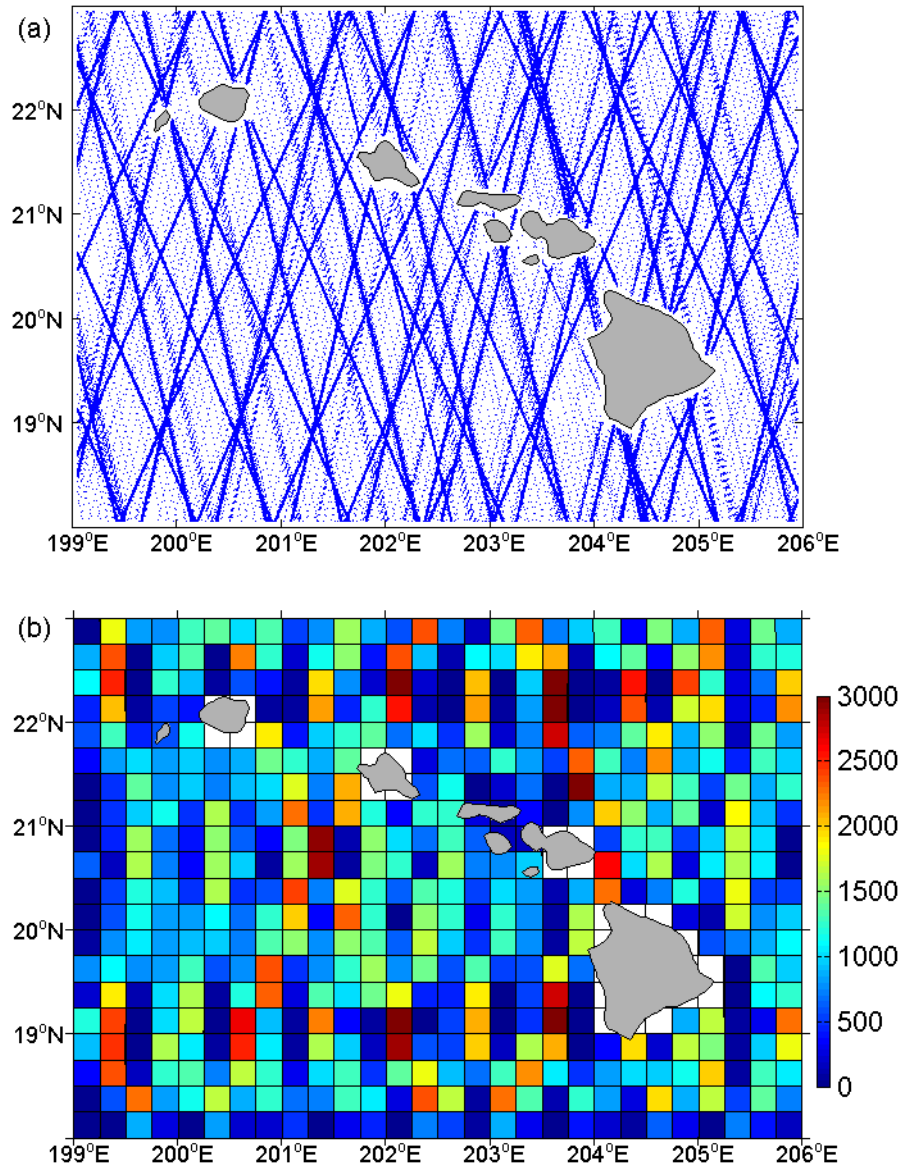


829

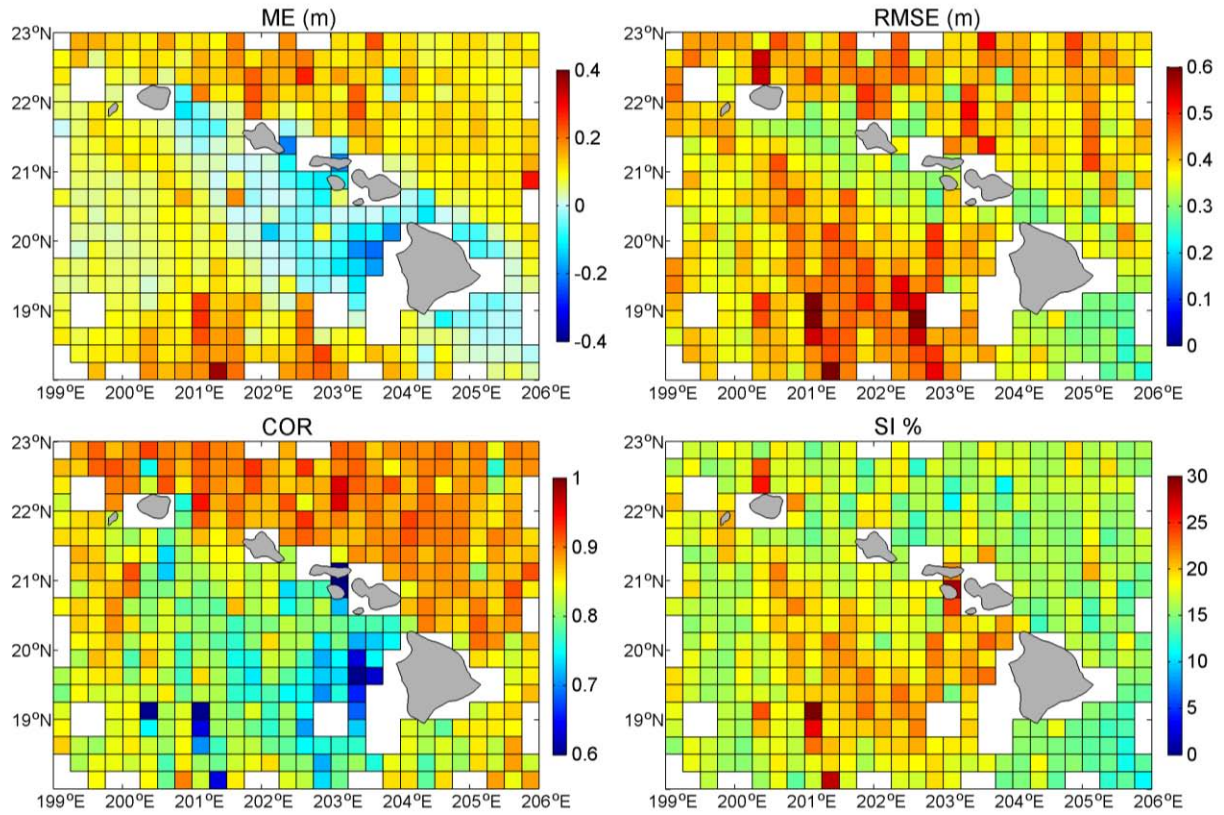
830 Figure 8. Error metrics of wind speeds from Hawaii WRF and QuikSCAT for 2000 to 2009.

831

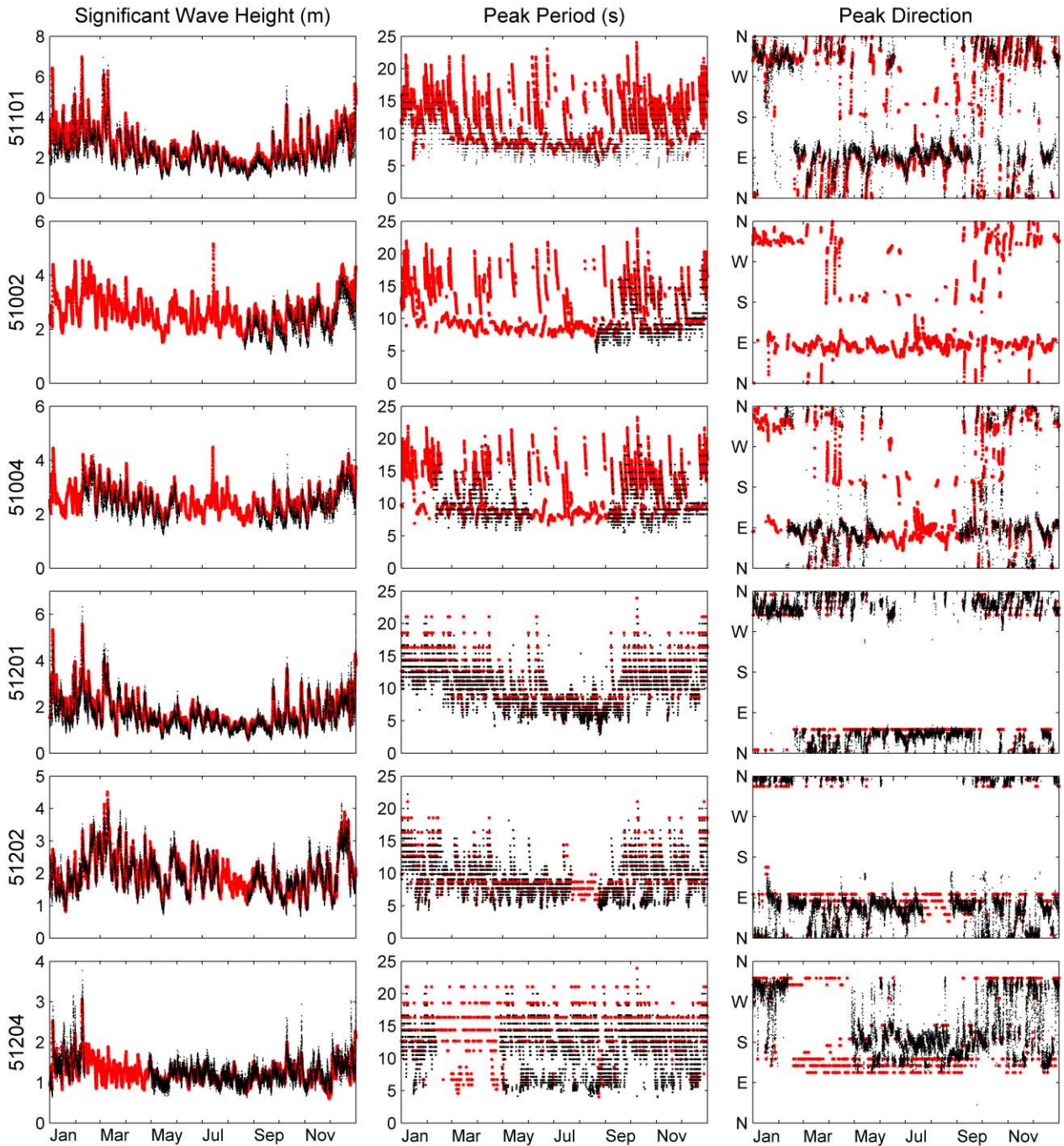
832



833  
 834 Figure 9. GlobWAVE altimetry observations around Hawaii from 1991 to 2011. (a) Track  
 835 distribution. (b) Number of observations per cell.  
 836

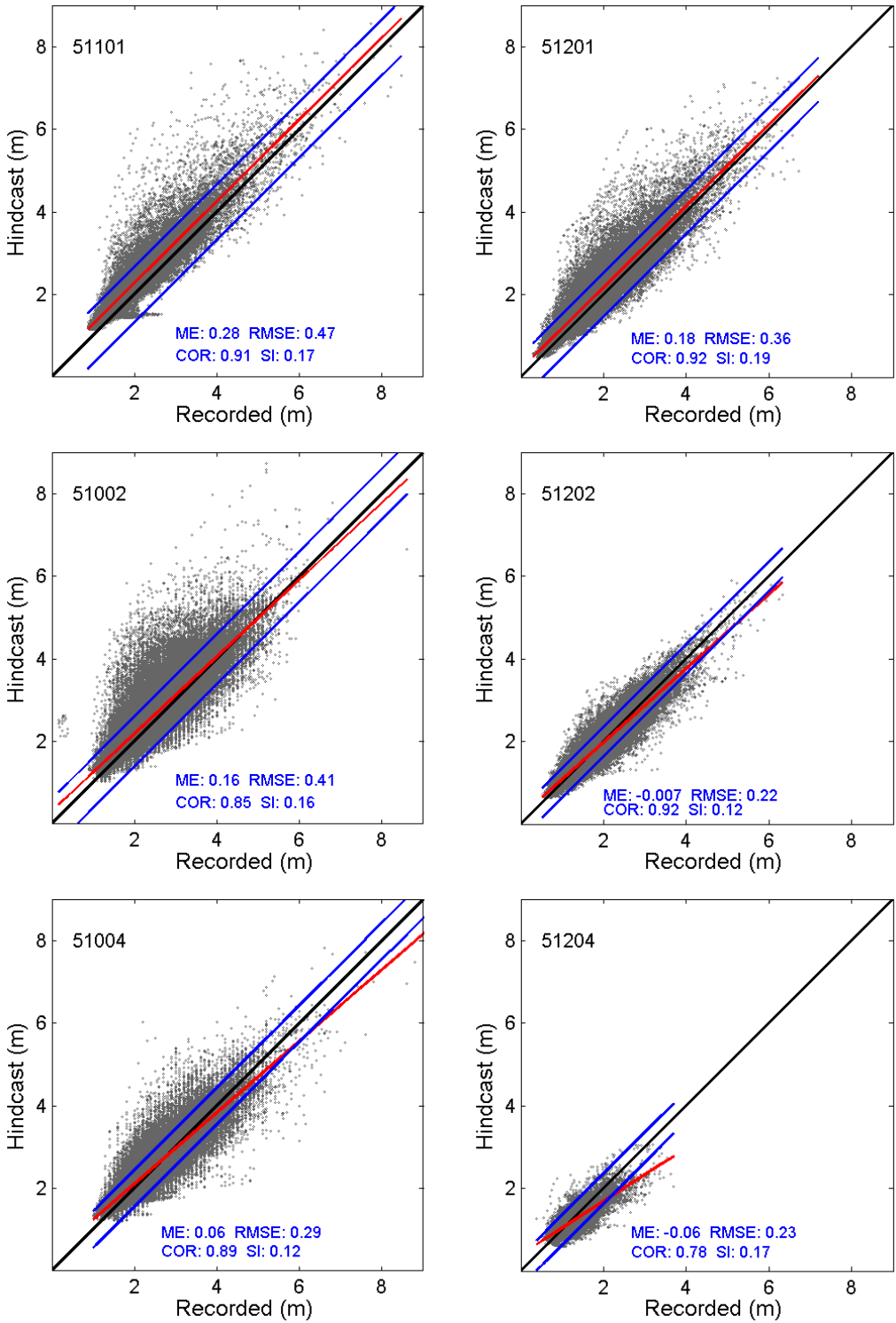


837  
 838 Figure 10. Error metrics of significant wave heights from Hawaii WAVEWATCH III and  
 839 GlobWAVE altimetry measurements for 1991 to 2011.  
 840



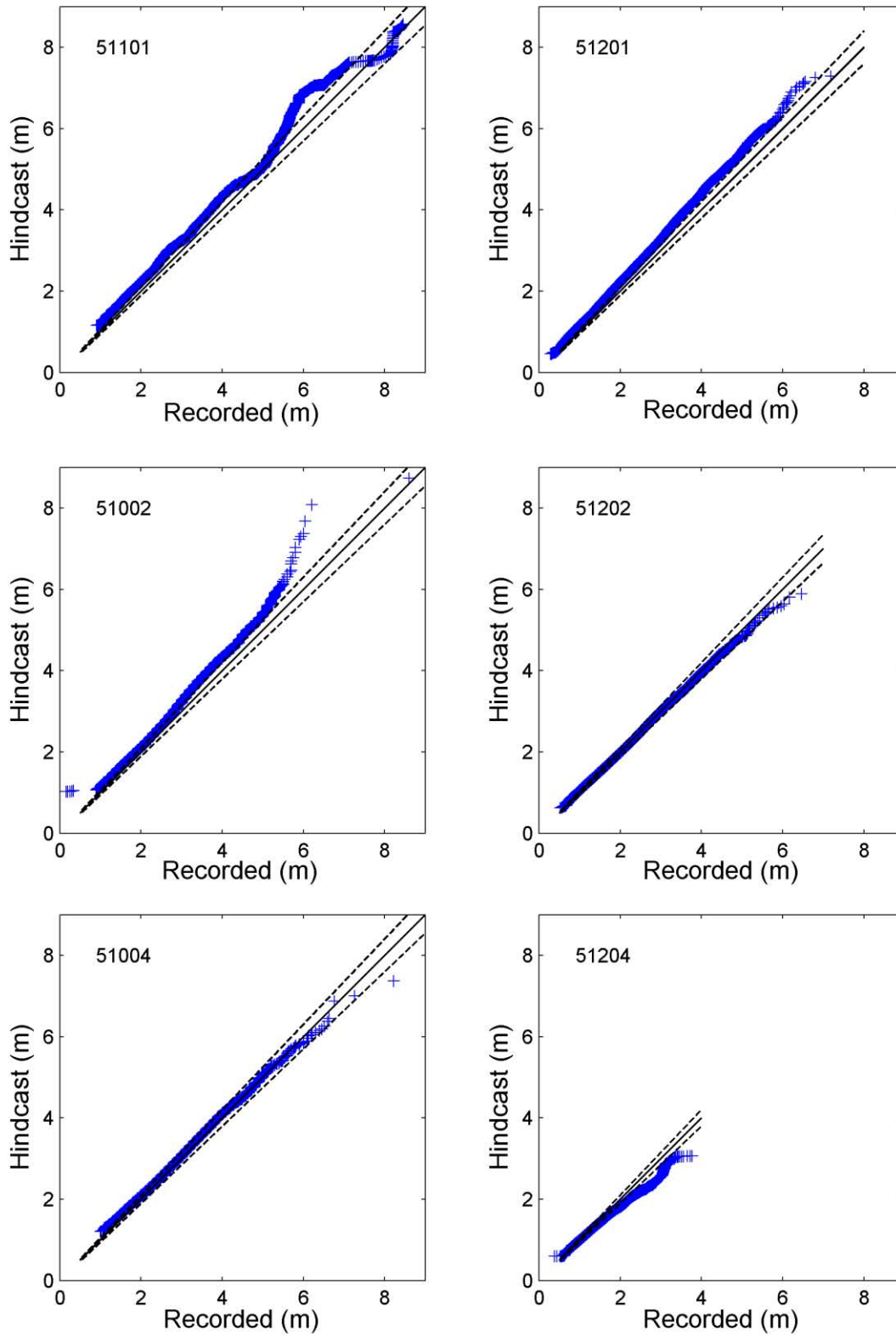
841  
 842  
 843  
 844

Figure 11. Comparison of recorded (black) and hindcast (red) wave parameters at selected offshore and nearshore buoys for 2012.



845

846 Figure 12. Scatter plots of hindcast significant wave heights and buoy measurements at selected  
 847 offshore and nearshore buoys. Black line denotes perfect match, blue lines delineate 90% of the  
 848 data, and red line is the linear regression.



849  
 850 Figure 13. Quantile-quantile plots of hindcast significant wave heights and buoy measurements  
 851 at selected offshore and nearshore buoys. Black line denotes perfect match and black dash lines  
 852 delineate the  $\pm 5\%$  error bounds.